Regional-scale InSAR investigation and landslide early warning thresholds in Umbria, Italy

Francesco Ponziani [a], Pierpaolo Ciuffi [b], Benedikt Bayer [c], Nicola Berni [a], Silvia Franceschini [c], Alessandro Simoni [b,*]

[a] *Regione Umbria Civil Protection Office - Functional Centre, Foligno, PG, Italy*
[b] *Department of Biological, Geological and Environmental Sciences (BiGeA), University of Bologna, Via Zamboni 67, 40126 Bologna, Italy*
[c] *Fragile s.r.l., Viale Fanin 48, 40127 Bologna, Italy*

ARTICLE INFO

ABSTRACT

In this work, we use conventional two-pass differential satellite interferometry for the investigation of active landslides at regional scale in the Umbria Region of Italy. First, we use InSAR for the detection of active slope movements during the study period (October 2019 to January 2021). Then, we characterize the displacement rates and their variation through time for selected active slopes, by analysing 6-days interferograms. The evolutionary trends of the phenomena are compared to the pertaining climate and soil parameters that are used by the regional landslide early warning system (LEWS) to predict the possibility of landslide occurrence over the territory. We aim to explore the potential of differential interferometry to detect and monitor active landslides and, through that, to validate a geographical LEWS:

Through the analysis of stacked interferograms, we identified 256 InSAR deformation signals (IDS) corresponding to active slope movements. Their distribution is compared to the geological map and the landslide inventory, illustrating how active landslides are favoured by weak lithologies and pre-existing slope instability. Also, the relative orientation of the satellite's line of sight with respect to the slope influences the results indicating a bias in the completeness of remotely sensed data. However, in the context of land management and civil protection, the results constitute a valuable information dataset for plans managed by local authorities.

The analysis, at the interferogram scale (6-days), of 13 clearly recognizable IDSs illustrates the dynamics of the slopes through the variation of the displacement rates. Due to decorrelation, only about half of the interferograms can be used for this purpose, and interpretation is required. The comparison to the alert thresholds of the Umbria region shows the remarkable relationship between InSAR-derived landslide activity and the parameters used for landslide prediction (i.e., 48 h rainfall and soil moisture conditions). The maximum 48 h cumulative rainfall and the soil saturation index prove effective to predict landslide reactivations and accelerations. We provide uncertainty measures of the landslide prediction through binary classification metrics. Such results are only preliminary, given the limited number of landslides and timespan of our dataset. However, it represents one of the few attempts to validate the forecast of a regional LEWS quantitatively.

1. Introduction

Landslides shape mountainous regions where they pose a relevant hazard to people and infrastructures resulting in hundreds of deaths and billions of dollars in damages every year (Kishore et al., 2018). However, given the widespread occurrence of relatively small but damaging events (Guzzetti, 2000), the economic consequences are difficult to estimate and tend to be underestimated. The combination of a rapidly increasing global population and the intensifying weather extremes associated with recent climate change suggests that landslide risk will dramatically increase over the next decades (Gariano and Guzzetti, 2016).

Given their complex physics and the diverse nature of triggering mechanisms (e.g., rainfall, earthquakes, frost cracking), documentation of landslide dynamics through monitoring is critical for hazard evaluation and risk management. Landslide deformation can be extremely slow

---

(a few millimetres per year) or involve sudden failure (Hungr et al., 2014), so their hazards include both enduring damage to manmade structures and catastrophic destructive events. While small landslides make up the vast majority of landslide events in any given year (Glade and Crozier, 2005), large landslides tend to be responsible for most damage and loss of life (Froude and Petley, 2018). In most regions of the world, the characterization of their locations and impacts is still problematic due to the variety of landslide types and morphologies and the difficulty of collating and updating inventories. It is thus important that we continue to develop tools and techniques to detect and monitor these gravitational slope processes.

Landslides can be mapped and monitored with field observations, digital elevation models, satellite and airborne imagery (Mantovani et al., 1996; Guzzetti et al., 2012; Chae et al., 2017). Remote sensing techniques combine the inherent advantages of their areal perspective with the remarkable precision of the more advanced radar-based methodologies (Cohen-Waeber et al., 2018). Furthermore, the number of satellite-based sensors is steadily increasing together with the frequency of acquisitions, making the observations more detailed in space and time (Mondini et al., 2021).

Interferometric processing of synthetic aperture radar images (InSAR) has proven useful to investigate gravitational slope movements both for specific landslide studies (Xu et al., 2020; Wasowski and Bovenga, 2014) and for regional analysis (Solari et al., 2020; Zhang et al., 2020). In the latter case, InSAR has been used not only for the detection of active landslides (Dini et al., 2019; Zhao et al., 2012) but also for deformation monitoring (Bekaert et al., 2020; Shi et al., 2020). However, the regional investigation of landslides through InSAR techniques is still challenging due to several factors. Landslide displacement detection and monitoring is not possible when snow cover is present while the presence of dense vegetation induces temporal decorrelation. Atmospheric delay anomalies, topographic artefacts (Liang et al., 2018; Murray et al., 2019) and decorrelation due to large deformation gradients (Hu et al., 2019; Manconi, 2021) are among the factors significantly influencing our ability to measure surface displacements. In addition, the satellite orbital geometry and the side-looking SAR imaging makes some slope orientations less favourable and causes layover and shadowing over steep mountainous terrain (Wasowski and Bovenga, 2014).

In the last decades, various interferometric techniques have been proposed to process multi-temporal SAR acquisitions over large areas. They can be grouped in two main families: standard InSAR methods that include classic two-pass interferometry and interferometric stacking (Dini et al., 2019; Handwerger et al., 2013, 2015) and multi-temporal methods that include the so-called Persistent Scatterer Interferometry (PSI) and Small Baseline Subsets (SBAS) methods (Raspini et al., 2019; Zhang et al., 2020). In general, multi-temporal methods allow obtaining better accuracy and precision for good quality reflectors (houses, infrastructures, rock outcrops) but standard InSAR yields a more continuous coverage of the territory also when sparse to medium vegetation cover is present.

Archived and newly acquired SAR images can be interferometrically processed to extract displacement time series. Their analysis can be used to determine the sensitivity of landslide motion to external factors such as seasonal precipitation and seismic shaking (Cohen-Waeber et al., 2018; Handwerger et al., 2015; Albano et al., 2018) and may have a significant potential in detecting precursory deformation preceding catastrophic failures (Dong et al., 2018; Ciuffi et al., 2021; Xie et al., 2020).

This work presents the results of a regional InSAR investigation performed by using standard differential methodologies and C-band Sentinel 1 SAR images. The Umbria region of central Italy is the study area (8456 km^2), and our analysis covers the period between October 2019 and January 2021.

We aim to detect and map active slope movements by analysing stacked interferograms. We also intend to use the phase information contained in single differential interferograms to monitor the slope deformation through time. The use of conventional two-pass interferometry is used to achieve a better territorial coverage compared to multi-temporal techniques and to detect landslide acceleration/decelerations with the highest possible frequency (6 days).

The work compares the location of detected InSAR deformation signals (IDS) to existing geological and geomorphological information to gain understanding of their correlation. Interferograms are used to describe the evolution of selected landslide whose state of activity is compared to rainfall and soil moisture parameters. The Civil Protection of the Umbria region uses such parameters to forecast landslide occurrence over its territory and issue alert bulletins. To our knowledge, this work represents one of the first attempts of using remotely sensed displacement data to support the calibration and validation of predictive methodologies for landslide early warning systems (LEWS). Encouraging results indicate that InSAR detection of actively moving landslides can be helpful for territorial surveillance and for the development of predictive tools for geographical LEWS.

2. The study area and the landslide early warning system

The morphology of the Umbria Region (8456 km^2), located in central Italy, spans from alluvial plains to hills and mountains, with elevations ranging from 50 to 2436 m a.s.l. (Fig. 1). The geology is dominated by the presence of sedimentary rocks with post-orogenic marine and continental facies, flysch deposits consisting of clay-schist and clay-marl sediments, well-bedded limestones and subordinate volcanic rocks (Cardinali et al., 2002). Agriculture/arable land covers about 54% of the territory, forest 32% urban areas account for about 5%.

Landslides are widespread and recurring: all municipalities in Umbria are exposed to some degree of landslide risk, and landslide deposits cover about 9% (650 km^2) of the area. According to the national inventory IFFI (Trigila et al., 2010), >70% of the 12,477 mapped landslides are dormant while the remaining are active, mostly based on geomorphological criteria.

The precipitation regime can be classified as Mediterranean. There are distinct dry and wet seasons, with Mediterranean-type precipitation regime, higher generally during the autumn-winter period when landslides and floods are more common. Mean annual precipitation is about 1000 mm; mean annual temperature is 11 °C; snowfalls at altitude below 500 m are sporadic and unusual.

In Italy, each region is in charge of monitoring, and forecast weather phenomena and weather-related natural risks in real time. The landslide early warning system (LEWS) of the Umbria region aims to predict conditions of local (first level alert) or widespread (second level alert) landslide occurrence over the territory which is divided in six alert zones (> 500 km^2) for this purpose. Landslide hazard scenarios are updated every 24 h and support the decision-making authorities with a first-order regional alert procedure.

Given the uncertainties inherent to landslide prediction (Chae et al., 2017), the daily forecast is based on simplified, empirical systems. Most methods rely on precipitation parameters, such as return time-based rainfall thresholds, or intensity-duration landslide triggering thresholds (Guzzetti et al., 2020; Peruccacci et al., 2017). Operational systems based on parameters other than rainfall are rare. The operational simplicity of these systems, however, can cause problems to Civil Protection duties. Switching from probabilistic forecasts with strong uncertainty to a decision-making procedure based on discrete alert levels can generate "wear" following false alarms or missed alarms.

In this context, the Umbria civil protection authorities implement the regional LEWS. The threshold methodology relies on measured/forecasted rainfall parameters and a Soil Saturation Index (SSI). Recent literature increasingly reports the key influence of soil saturation as a parameter of primary importance in landslide triggering processes (Lazzari et al., 2018; Wicki et al., 2020; Bezak et al., 2021). The 48-h rainfall parameter has a resolution of 1 km and is obtained through a merging procedure combining radar reflectivity and rain gauges
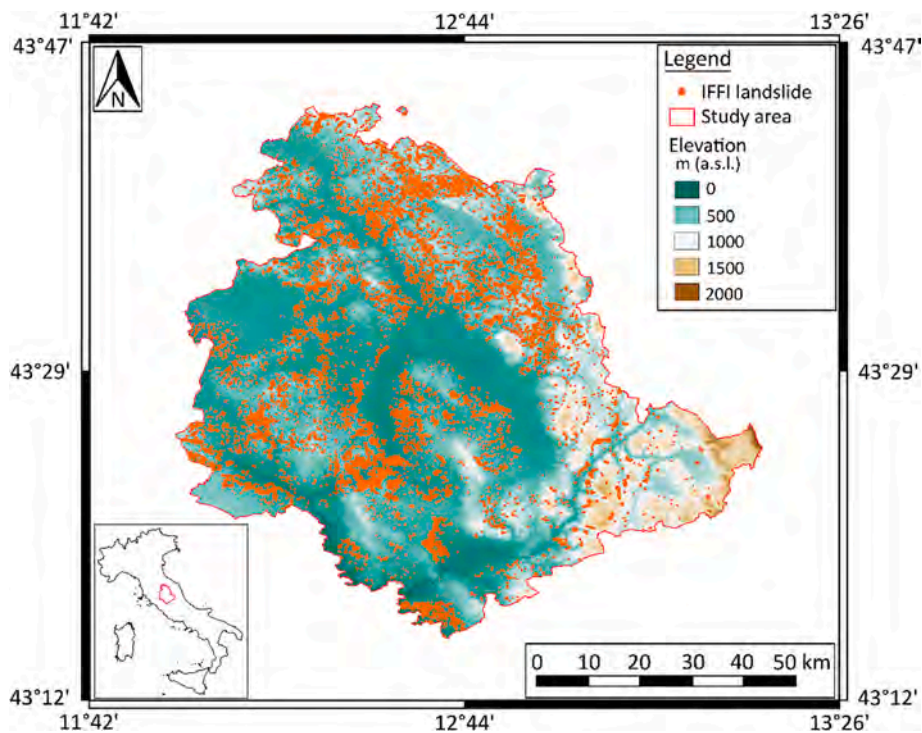
Fig. 1. Schematic elevation map of Umbria Region and distribution of the landslides mapped by the IFFI inventory.

(Sinclair and Pegram, 2005; Bruno et al., 2021). The calculation of SSI is based on distributed precipitation measurements and a soil water balance model (Brocca et al., 2010a; Silvestro et al., 2013, 2015) calibrated against experimental monitoring data (i.e., soil moisture probes network, river discharge, ASCAT satellite wetness index) as described by Brocca et al., 2010b. Our threshold-based methodology uses SSI to estimate the water content of the soil at the beginning of the landslide triggering rainfall. The SSI implicitly takes into account the pattern and space-time distribution over the territory of antecedent precipitation, simplifying the description of triggering rainfalls. Using information available on landslides inventories, Ponziani et al. (2012) studied the correlation between SSI and maximum cumulated rainfall values during landslide events. Results highlighted that the introduction the soil moisture index leads to an improvement in data dispersion, therefore to a lower uncertainty (i.e., lower false and missed alarms numbers).

Based on the comparison between predicted parameters with the first and second level alert thresholds, the operational Umbria LEWS issues daily bulletins describing the evolution of weather phenomena and associated landslide alert levels for a grid of 750 point distributed over the entire regional territory.

3. Materials and methods

3.1. InSAR analysis and active landslide mapping

We use a traditional two-pass interferometry approach to process SAR images acquired by Copernicus Sentinel 1 A/B satellites. The Sentinel images are C-band images (5.6 cm radar wavelength) acquired every six days (interval between Sentinel 1 A and Sentinel 1B).

Our analysis spans between October 2019 and January 2021 and considers one descending and one ascending orbits, each with two sub-swaths. We divided the relatively vast Umbria region (8456 km^2), in 7 sub-basins that were separately processed. Geocoding and interferogram processing are performed by means of GMTSAR InSAR package (Sandwell et al., 2011) while complex interferograms were unwrapped with SNAPHU (Chen and Zebker, 2001). We produced 1120 interferograms with temporal baseline in the range 6 to 24 days.

The topographic phase was calculated and subtracted (e.g., Massonnet and Feigl, 1998; Bürgmann et al., 2000) by using an external digital elevation model (10 × 10 m up to elevation = 200 a.s.l. and SRTM above). Large scale atmospheric noises have been reduced by high pass filtering the interferograms and by selecting a stable reference area: we typically chose geomorphological features (e.g., ridges) that are not involved in gravitational movements. Goldstein filters (Goldstein and Werner, 1998) have been applied to reduce residual noises and enhance the deformation signal.

We identified actively moving landslides by stacking interferograms and then crosschecking our results with the morphology of the slopes and with recent aerial photographs. Interferogram stacking improves the signal to noise ratio and highlights features moving at a rate sufficient to observe deformation in a short time span, yet slow enough to avoid loss in radar coherence. The interpretation of interferometric stacks led to the identification and mapping of InSAR deformation signals likely caused by landsliding, that we refer to as IDS, in the following.

In compiling our IDS inventory, we excluded signals extending across rivers or mountain crests, and, whenever we encountered dubious signals, we inspected single interferograms to check for possible residual topographic or atmospheric errors which may generate artefacts. Typically, our deformation signals show a sign inversion of the movements measured by the ascending and descending orbits, which is consistent with a downslope deformation, especially when the slope gradient is gentle and the along-slope displacement dominant. Similar approaches were used for areal investigation of active slope movements by other authors (Handwerger et al., 2015; Ciuffi et al., 2021; Tong and Schmidt, 2016).

3.2. Analysis of InSAR results: spatial distribution of InSAR deformation signals

We compared our IDS inventory to four simple geological and geomorphological control elements: bedrock lithology, slope gradient, exposure and landslide inventory. The aim is to detect significant correlation with each control element and, therefore, to improve our

understanding of the spatial distribution of the signals over the territory. In order to do so, we adopted an established approach (Meyer et al., 2014; Regmi et al., 2010) to evaluate the topographical predictability of landslides. The technique is based on the theory of weights of evidence (WOE). WOE is a data-driven method (Bonham-Carter, 1994), which is basically the Bayesian approach in a log-linear form (Spiegelhalter, 1986) and uses prior (unconditional) probability and posterior (conditional) probability. In order to get more information about the analysis, there are papers available in the literature that explain the methodology in detail applied in different geological contexts such as Regmi et al., 2010 and Meyer et al., 2014.

The control elements and the classes used for the analysis are reported in Table 1. The classes of bedrock lithology are obtained by grouping Geological Formations (Pialli et al., 2009) based on their age and expected geomechanical behaviour. The landslide inventory control element considers the presence of a mapped landslide in the national inventory and its inferred state of activity (IFFI, Trigila et al., 2010).

The rasters of the 4 control elements were intersected with the deformation signal inventory. For each class j of the control elements V_i (with $j = 1…n$), we evaluated the number of cells corresponding to the four possible combinations (Table 2). The values are used as input data for the computation of the Contrast (C): a statistical parameter that expresses the degree of correlation between a given factor (the class of a control element, $V_{i,j}$) and the dependent variable (in our case the deformation signals).

The Contrast is obtained from the difference of the weights $W^+_{i,j}$ e $W^-_{i,j}$:

$$C_{i,j} = W^+_{i,j} - W^-_{i,j} \qquad (1)$$

where

$$W^+_{i,j} = log\left\{\left[N_{pix1}/(N_{pix1}+N_{pix2})\right]/\left[(N_{pix3}/(N_{pix3}+N_{pix4}))\right]\right\}$$

$$W^-_{i,j} = log\left\{\left[N_{pix2}/(N_{pix1}+N_{pix2})\right]/\left[(N_{pix4}/(N_{pix3}+N_{pix4}))\right]\right\} \qquad (2)$$

$W^+_{i,j}$ expresses the probability of finding a given class ($V_{i,j}$) in a deformation signal. Conversely, $W^-_{i,j}$ expresses the degree of anti-correlation of such class with the dependent variable. If the Contrast is positive (C > 0), the class of the control element is favourable for the development of a deformation signal; if the Contrast is negative (C < 0), it is unfavourable.

In our case, when the value of Contrast is small, the significance of the correlation is uncertain because the deformation signals occupy a very small portion of the study area. Similarly, uncertainty can occur because a certain class of a given control element (e.g., carbonatic rocks of the bedrock lithology) is poorly represented in the considered territory. It is therefore inevitable that the Contrast is affected by an uncertainty that complicates its interpretation.

In order to get an estimate of the uncertainty associated to the Contrast, we use a bootstrapping technique consisting in the generation of N synthetic rasters of random polygons whose size and total area are

Table 1
Control elements and classes used for analysis.

Control elements	Classes
Bedrock lithology	1) Quaternary deposits
	2) Carbonatic rocks
	3) Plio-Pleistocene coarse deposits
	4) Plio-Pleistocene fine deposits
	5) Sandstone terrigenous deposits
	6) Predominantly pelitic and/or chaotic terrigenous deposits
Landslide inventory	1) No landslide
	2) Relict landslide
	3) Active landslide
	4) Dormant landslide
Slope gradient	7 classes of 5° width (2.5° to 37.5°) + 8th class for higher values
Aspect	8 classes of 45° width

Table 2
Intersections performed between InSAR deformation signals and classes of control elements.

|		Control elements ($V_{i,j}$)	
		Present (1)	Absent (0)
Deformation signal	Present (1)	N_{pix1}	N_{pix2}
	Absent (0)	N_{pix3}	N_{pix4}

similar to the InSAR-detected deformation signals. Each synthetic raster is then cross-referenced with the control elements (Table 1) and Contrast is calculated (N values of the Contrast for each class of the control element, $V_{i,j}$). Finally, the standard deviation of the Contrast is calculated for each $V_{i,j}$. Such standard deviation represents the statistical variability of the Contrast that is used to describe the uncertainty associated to the Contrast calculated for the actual deformation signals. Whenever the Contrast, despite the associated uncertainty, is greater (or smaller) than zero, the control element is positively (or negatively) correlated to the presence of deformation signals. If the uncertainty band straddles zero, out data show no significant correlation.

3.3. Analysis of InSAR results: velocity time series of selected deformation signals

The aim of this analysis is to obtain velocity information for selected IDSs. 13 clearly recognizable and sustained deformation signals were selected, among those mapped in stacked interferograms, based on the visual inspection of 6-days single interferograms.

The maximum temporal resolution of InSAR-derived measures is 6 days (satellite revisit time), and we use 6-days interferograms to extract the displacement rates of the 13 selected IDSs. Depending on the geometry of the slope, we use interferograms derived from SAR images acquired in ascending or descending orbit. In order to compensate for the relative orientation of the slope and the line-of-sight (LOS), we convert LOS displacement in downslope displacement, by assuming that the movement is parallel to the slope (Hilley et al., 2004).

We use the 75th percentile of the downslope displacement measured by single 6-days interferograms to estimate the velocity (V_{75}) of the selected deformation signals through time (Fig. 2). Highly decorrelated interferograms were discarded based on visual inspection, and "no value" is assigned to the displacement rate of the corresponding period. Decorrelation may derive from very different conditions: large ground displacements (> 1/2 wavelength which corresponds to 2.8 cm approx., in case of C-band Sentinel 1 data), technical errors (i.e., orbital and DEM inaccuracies), reflective properties change (i.e., plowing of agricultural fields), and others (Wasowski and Bovenga, 2014). We refer to the resulting time series as InSAR-derived velocity time series ($V_{75}TS$). Given that numerical velocity values derived from interferograms can be affected by uncertainty (i.e., residual noise from topography, atmosphere, and temporal decorrelation), we combine velocities with the interpretation of the signal. More particularly, we introduce the binary classification of landslide activity based on a limit value of V_{75}. The value of the limit derives from the visual interpretation of the interferograms: it distinguishes "active state" (i.e., deformation signal clearly recognizable) and "inactive state" (i.e., deformation signal weak or absent). Examples will be presented in Section 4.3. Based on the interpretation of the interferograms for each case analyzed; the V_{75} classification limit value varies between 30 mm/yr and 180 mm/yr for all selected cases. The use of different thresholds is required because the relative orientation of LOS and displacement vectors influences the numerical value of the displacement rate and because the dynamics of landslides is inherently different.
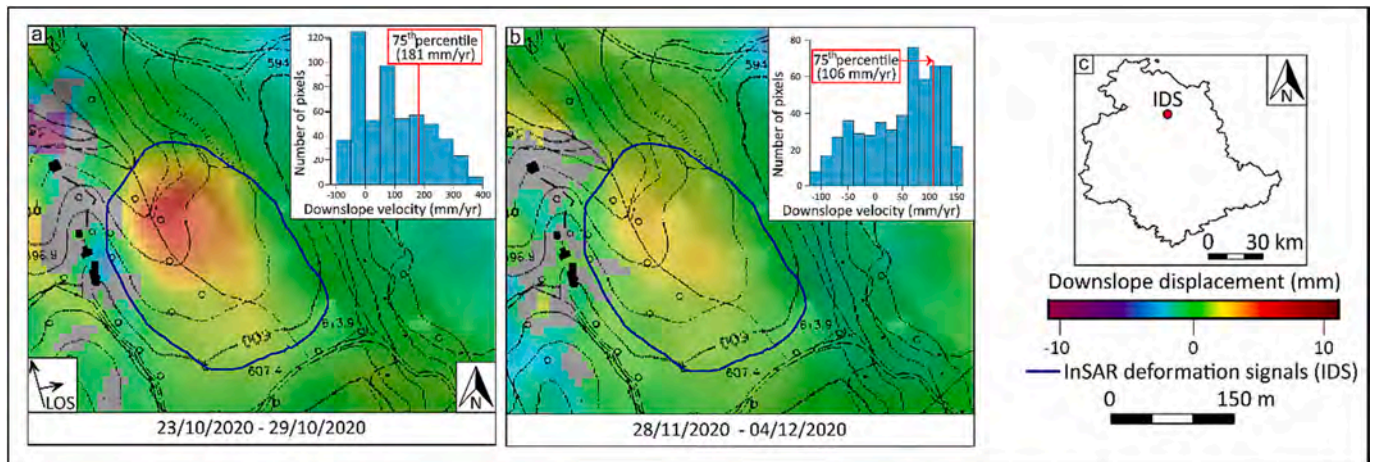
Fig. 2. 6-days interferograms describing the evolution of an example IDS. The IDS polygon is drawn based on stacked interferograms. Insets show the frequency distribution of the downslope-projected displacement rate inside the polygon. The displacement rate is evaluated in each interferogram by using the 75th percentile. Location of the example IDS on the regional territory shown on the right.

3.4. Comparison between landslide velocities, rainfalls and soil saturation index

InSAR-derived velocity information (V_{75}) have maximum nominal resolution of 6 days. Such information includes some missing values. In fact, when highly decorrelated, interferograms are discarded and no velocity information is retrieved. The date of acquisition of the later SAR image, used to generate the 6-day interferogram, is assigned to available V_{75} values.

Given rainfall measurement and soil saturation index have higher resolution than V_{75}, we need to downsample to allow comparison. First, we extracted 48-h rainfalls and SSI into the nearest grid points to selected IDSs. Then, we selected the maximum 48-h cumulated rainfall (max48rain) and the minimum soil saturation index (SSI) recorded
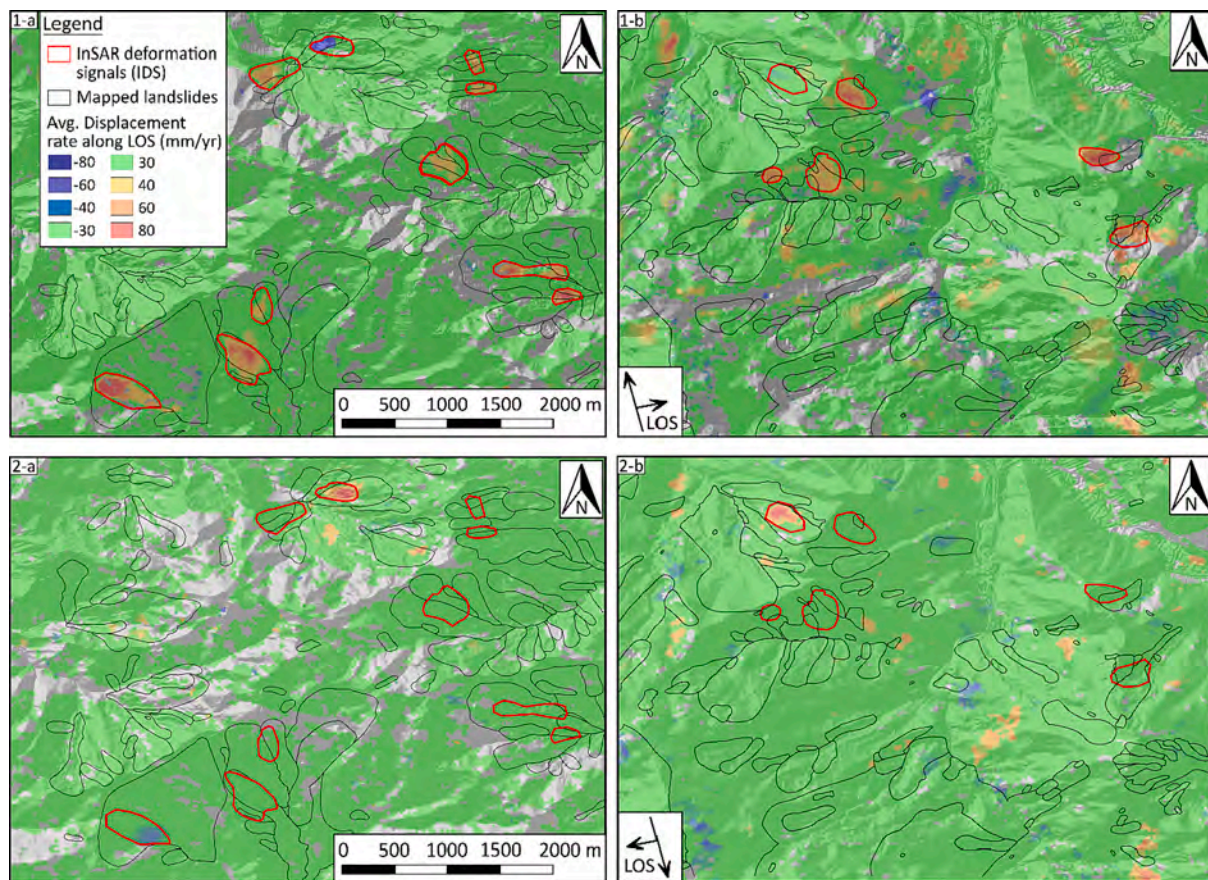
Fig. 3. Two example areas of the interferometric stacks obtained in ascending (1a-b) and descending (2a-b) geometry for the Umbria region (see location in Fig. 4) encompassing the period of analysis (01/10/2019 to 31/05/2020). Stacks are used for recognition and mapping of InSAR deformation signals. Displacement rates in the range − 30 to +30 mm/yr are considered too low to be detectable by our analysis, therefore shown in green colour. (For interpretation of the references to colour in this figure legend, the reader is referred to the web version of this article.)

during the corresponding V_{75} time window (6 days). In case of rainfall events longer than 48 h, only the highest value of rainfall cumulated over 48 h is used together with SSI at the onset of the rain.

To take into consideration the possibility that the "active state" exhibited by a IDS (cfr. Section 3.3) could be caused by rainfalls occurred before the beginning of the pertaining time window, we check the rainfall pattern of active IDSs associated to scarce or no rain (< 10 mm/48 h). If a larger rainfall episode is recorded in the previous time window, we consider such rainfall, and the corresponding preceding SSI, as associated to the landslide velocity information of the following time window.

Our methodology is designed to allow comparison between InSAR-derived landslide velocities and meteorological parameters used for territorial landslide early warning.

4. Results

4.1. Regional InSAR analysis

We recognized active landslides by stacking interferograms (i.e., time-averaged deformation) over the entire investigation period (October 2019 to May 2020). Stacking enhances the signal-to-noise ratio and highlights features that are persistent in time and space.

Fig. 3 shows two portions of the analyzed area where deformation signals are mapped based on the interferometric stacks. These latter show good coverage of the territory with decorrelated areas (i.e., grey areas in Fig. 3) mostly located along steep, heavily vegetated slopes. InSAR deformation signals that we associate to active landslides are typically patches with relatively high LOS velocity and high standard deviation of LOS velocity. Furthermore, the comparative analysis of the interferometric stacks derived from the two orbits reveals that IDSs show very often the sign inversion of the displacement. The inversion is compatible with displacements whose horizontal component prevail over the vertical, such as sliding along a moderately inclined slope. We

didn't find signal inversion in any other deformation signal except in landslides. Finally, we verified our IDSs with local morphology in aerial photographs and shaded relief map.

Overall, we identified 252 active landslides across the mainly hilly and mountainous territory of the Umbria region (Fig. 4). The deformation signals have planform area ranging from 0.01 to 0.5 km^2 approx., with an average of 0.07 km^2. The majority of IDSs (166) are recognized in landslide deposits mapped by the Landslide Inventory (Trigila et al., 2010). In this case, they indicate the active state of the entire landslide or of a part of it. Otherwise, IDSs are located along slopes where landslide features are not recognized nor mapped, indicating either first-time impending slope failures or the reactivation of previously undetected landslides.

4.2. Spatial distribution of InSAR deformation signals

The IDS inventory shows an uneven distribution over the territory. By comparing the spatial distribution of IDSs with four control elements (Table 1), we obtain an objective measure of their correlation. The results are expressed by the value of Contrast [1] in Fig. 5. Contrast is calculated for each class of the control elements and the associated uncertainty estimated by means of a bootstrapping technique (Section 3.2).

The results are coherent with the basic geological and geomorphological characteristics of the area.

The bedrock lithology has a strong influence on the distribution of active slope movements identified by IDSs. Pelitic/chaotic terrigenous deposits (class 6 in Fig. 5a) is the type of substratum most favourable to their occurrence. In this case, the value of Contrast is highest, demonstrating the relative abundance of active slope movements along the slopes made of fine-grained weak rocks. Positive correlations are also found for recent, Pliocene-Pleistocene, fine deposits (class 4) and Sandstones (class 5). Significant negative correlation is obtained for classes 1 and 2, corresponding to quaternary deposits (class 1) and
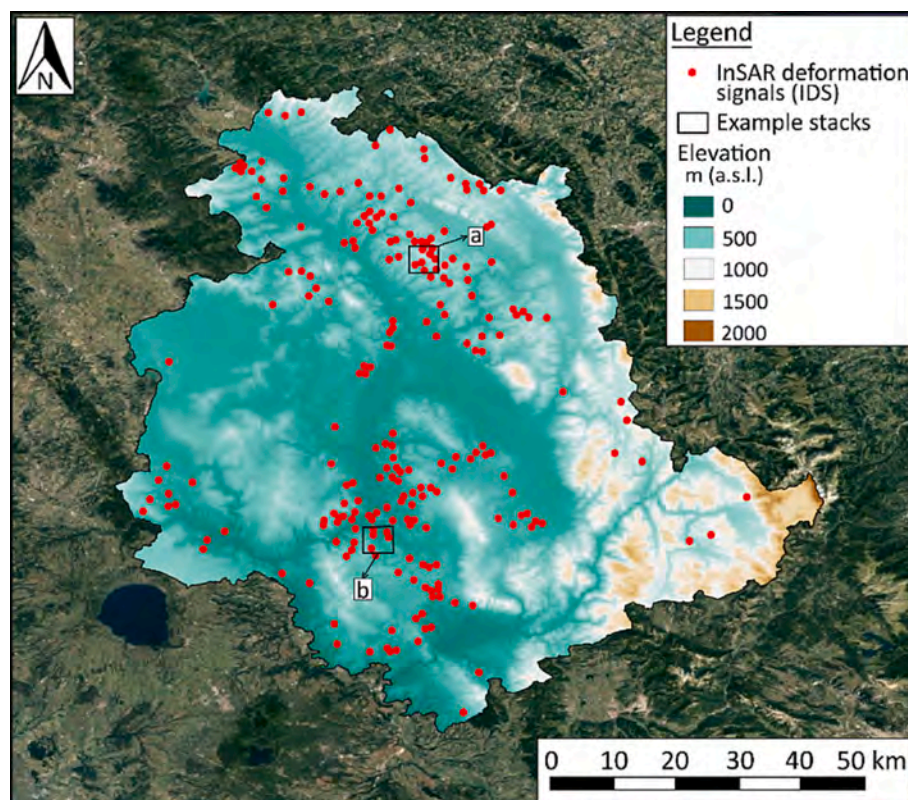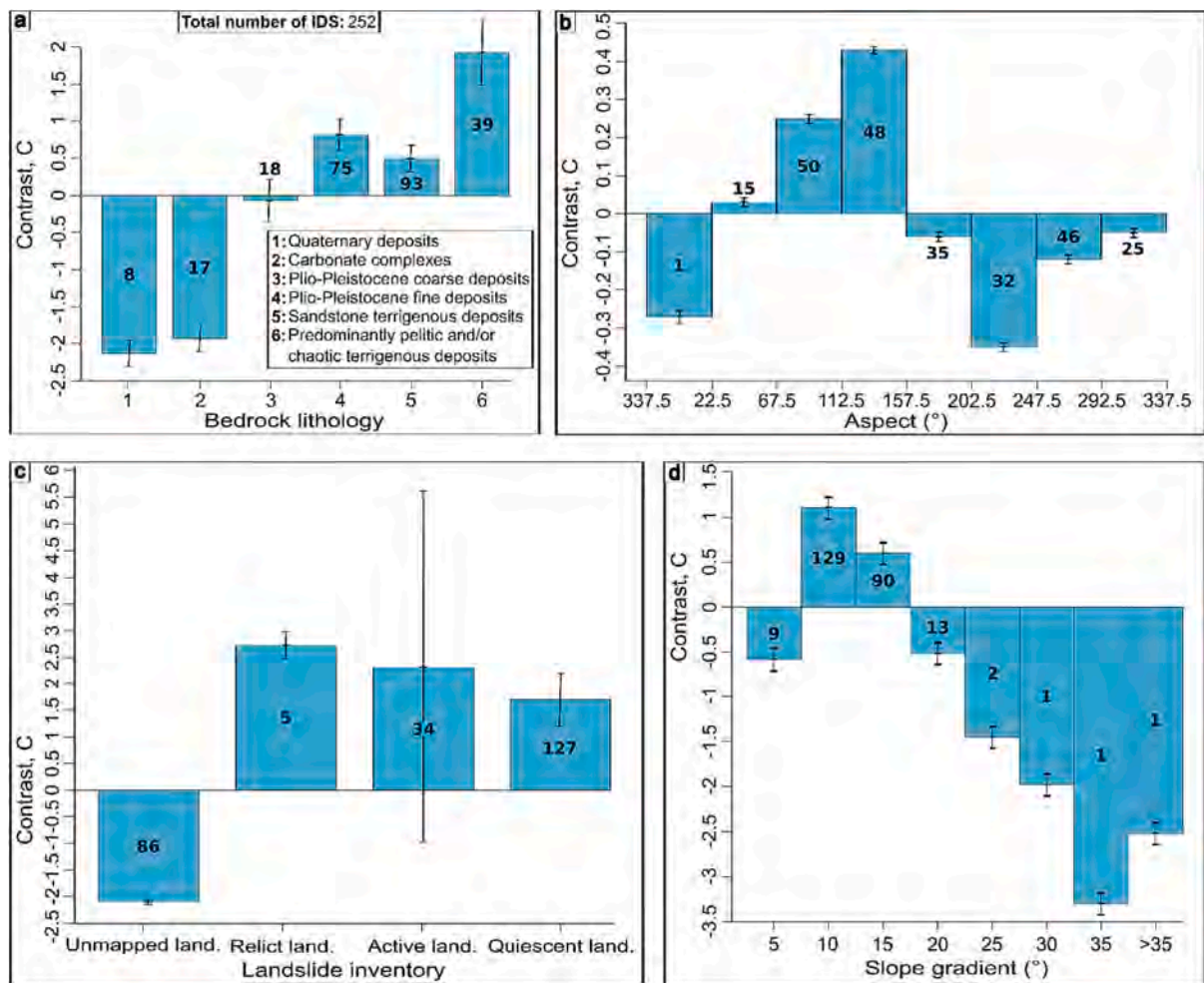

Fig. 4. Elevation map of Umbria and spatial distribution of InSAR deformation signals (IDSs) within Umbria region.

Fig. 5. Values of Contrast (C) obtained for the classes of the control elements. Positive values describe the spatial correlation between the class and IDSs. Error bars indicate the uncertainty associated to the correlation measure, numbers in the histograms indicate the abundance of InSAR deformation signals (IDS) for each class.

carbonate complexes (class 2). In this case, the values of Contrast capture the good stability conditions of the slopes made of carbonatic rocks and the low gradients of the slopes made of young sedimentary deposits.

The aspect of the slope (Fig. 5b) has a positive correlation mainly for slopes facing East while it is negative for the remaining classes. The trend of the Contrast values may indicate the conditioning of the geometry of SAR acquisition that makes displacements more problematic to measure when they occur along North or South facing slopes. In this cases, along-slope displacements have a smaller component of displacement along the satellite LOS compared to East and West facing slopes.

By comparing IDSs with the landslide inventory, we get positive correlation (C >> 0) with mapped landslides (Fig. 5c), regardless of their inferred state of activity (active, quiescent, relict). The opposite is found for the slopes where landslide deposits are absent.

The spatial correlation with slope gradients (Fig. 5d), indicates that the signals are more abundant along moderately steep slopes (7.5° to 17.5°) while the negative correlation becomes progressively stronger for higher gradients. The result is consistent with what we obtained for the bedrock lithologies since moderately steep slopes made of fine-grained weak rocks are the most susceptible to landsliding in Umbria.

4.3. Interferogram interpretation and evolution of IDSs through time: some examples

Although stacking interferograms proved very useful to recognize

and map meaningful deformation signals, single interferograms potentially yield information about the evolution of the phenomena through time. Given they are also prone to include the effects of residual noise (Yunjun et al., 2019) and temporal decorrelation (Zebker and Villasenor, 1992), visual expert interpretation is required to extract relevant information (Manconi, 2021).

Here, we illustrate three examples of the 13 IDSs that we selected for time series retrieval. The scope is to give the reader a better idea of the information contained in single interferograms and associated uncertainties.

Example 1. Case Basse.

The InSAR deformation signal of Case Basse do not correspond to a mapped landslide (IFFI, National Inventory of Landslides). The movement involves fine deposits of Plio-Pleistocene age along a gently dipping slope (9.2°) facing East. Interferometric results, shown in Fig. 6, document slow movements peaking towards the end of the analysis period (December 2020) when our velocity estimates reach values of about 800 mm/yr. Single interferograms (Fig. 6b, c, f, g) show artefacts, in the form of local negative values of downslope displacements which do not prevent recognition of the deformation signal generated by the gravitational movement. Such artefacts can derive from residual topographic or atmospheric errors. The velocity time series (Fig. 6) show active state prevailing during the cold season (Fig. 6b, c, e) and weak to absent deformation signal during summer (Fig. 6a, d). The activity threshold is placed at 80 mm/yr (see Section 3.3). During spring, there is
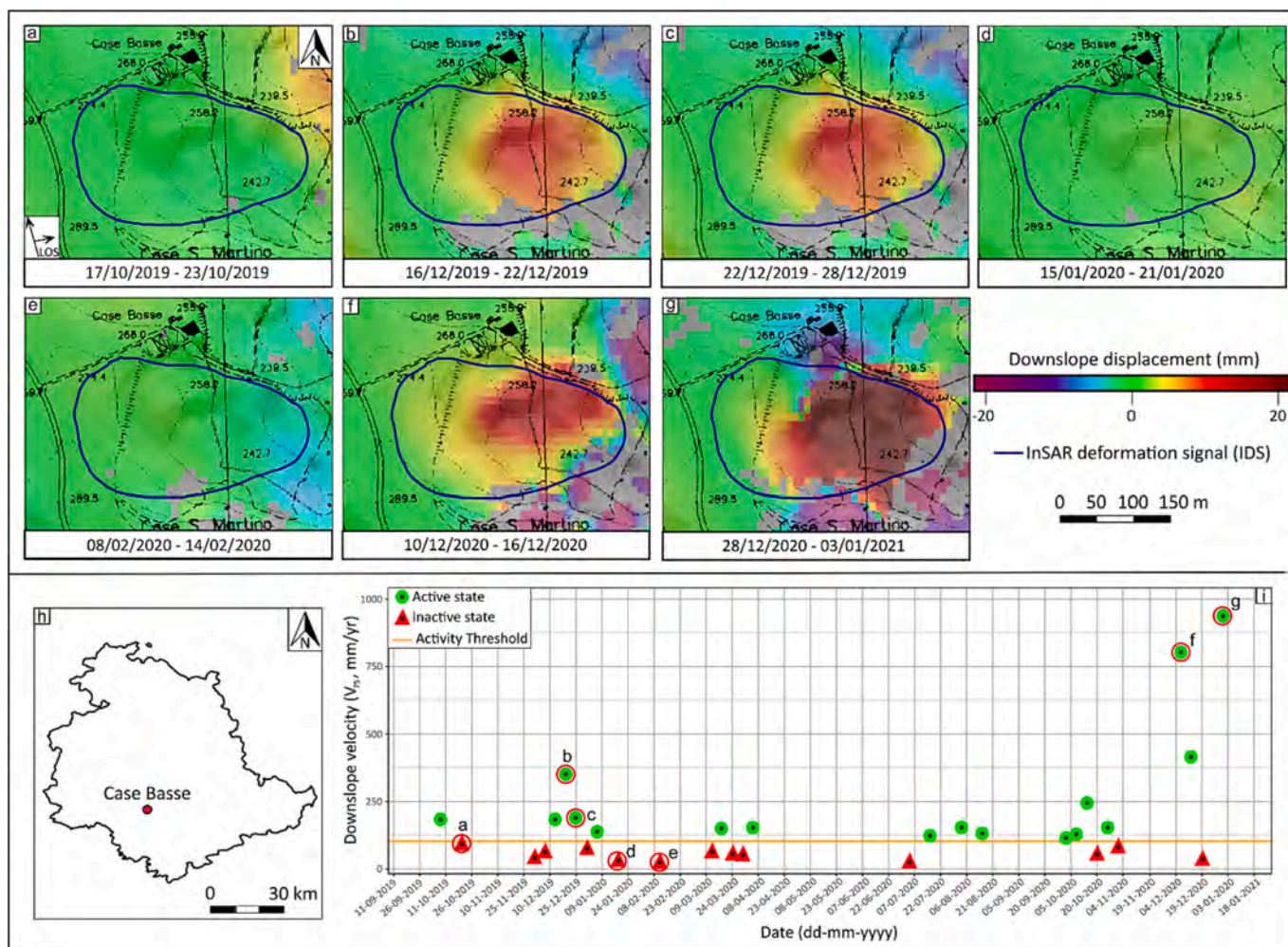
Fig. 6. Example interferograms obtained for the Case Basse IDS illustrating different states of activity (a-g). Velocity time series (i) reports V_{75} obtained from interferograms. Symbols with labels refer to the example interferograms. Location of the landslide on the regional territory shown at the bottom left (h).

a no-data period due to high decorrelation caused by rapid vegetation growth and/or by agricultural processing (temporal decorrelation). In all the interferograms, the highest deformation rates are located in the lower part of the slope (260 to 235 m a.s.l.).

Fig. 7 shows the IDS draped over aerial photography and a UAV

photo showing the irregular morphology of the landslide deposit, despite agricultural processing.

Example 2. Coldivecchio.

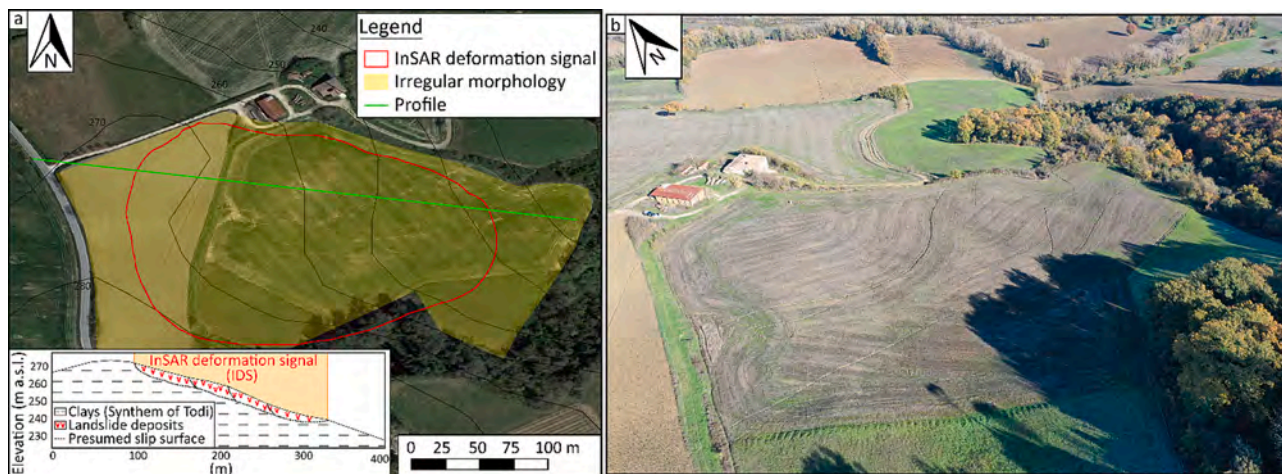Similarly to the first example, Coldivecchio is not mapped in the

Fig. 7. UAV (Unmanned Aerial Vehicle) photograph of the "Case Basse" slope. Within the cultivated field in the centre of the photo, the irregular morphology of the slope and the presence of a surface water network are recognizable.

National Inventory of Landslide (IFFI). The slope movement involves Sandstone terrigenous deposits of Miocene age belonging to the Member of Galeata (Pialli et al., 2009) along a moderately dipping slope (9.3°) facing NW.

Interferograms (Fig. 8) document high displacement rates at the end of the analysis period, during December 2020. The highest velocity of 560 mm/yr is recorded between December 4th and 10th and the corresponding interferogram is shown in Fig. 8d. Interferograms "a", "b" and "e" are not plotted within the time series and this, because they record displacement values below our threshold of 80 mm/yr. The velocity time series (Fig. 8) shows multiple stages of slope movement activity, separated by relatively long stages of little or no movement (inactive state). During the spring-summer period, between April and September 2020, highly decorrelated interferograms do not allow for a meaningful estimate of the displacement rate at Coldivecchio, likely due to rapid vegetation growth and agricultural practices. Also, in this case, the NW exposure of the slope is not favourable to InSAR, especially in descending orbit.

During the active state, higher velocities are recorded at lower elevations, but deformations involve the whole IDS. Field surveys identified the landslide-related irregular morphology of the slope (Fig. 9) and demonstrated that the road running in the crown area is also interested by notable deformation (Fig. 9b).

Example 3. Montanaldo.

The landslide of "Montanaldo" is mapped in the National Inventory of Landslide Phenomena (IFFI). It involves pelitic and/or chaotic terrigenous deposits belonging to the Olistostromes of the Galeata member (Pialli et al., 2009), of Miocene age. The average slope and aspect are 8.5° and 278°, respectively. By comparing the IDS (Fig. 10) with the mapped landslide (IFFI landslide), Fig. 11 shows how the deformation signal is located in the lower portion of the mapped landslide, extending beyond its lateral margins and toe.

The Montanaldo IDS shows velocities peaking in the cold season with maximum values at the end of 2020. Example interferograms (Fig. 10) show very variable displacement rates at Montanaldo with peak values of about 800 mm/yr at the end of 2020 (Fig. 10f, g). The slope movements at Montanaldo are generally sustained with occasional above-threshold deformations also during spring and summer. In this case, some good quality interferograms allow for velocity estimates also
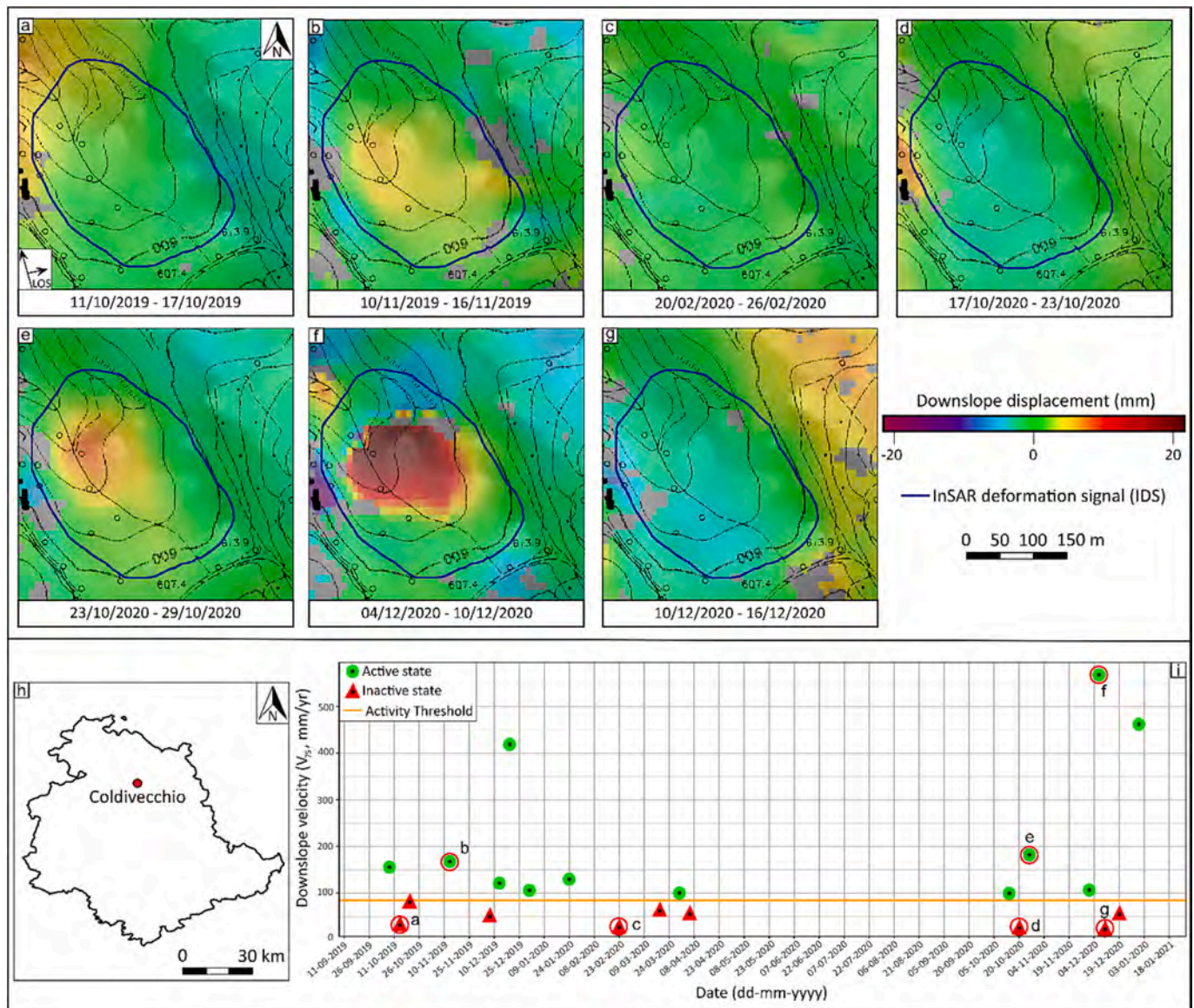
Fig. 8. Example interferograms obtained for the Coldivecchio IDS illustrating different evolution states of activity (a-g). Velocity time series (i) reports V_{75} obtained from interferograms. Symbols with labels refer to the example interferograms. Location of the landslide on the regional territory shown at the bottom left (h).
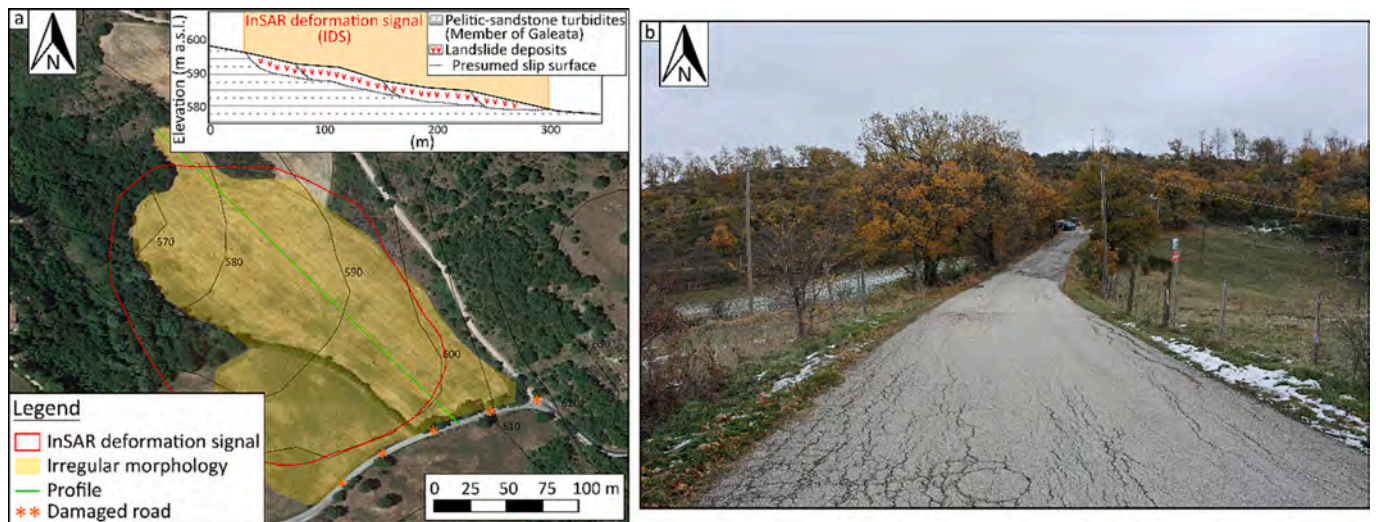
Fig. 9. Detail of undulating and cracked road for the case study "Coldivecchio". The deformed road shown is the one recognizable within Fig. BB, within the series of interferograms, located at higher elevations (approximately 608 m a.s.l.).
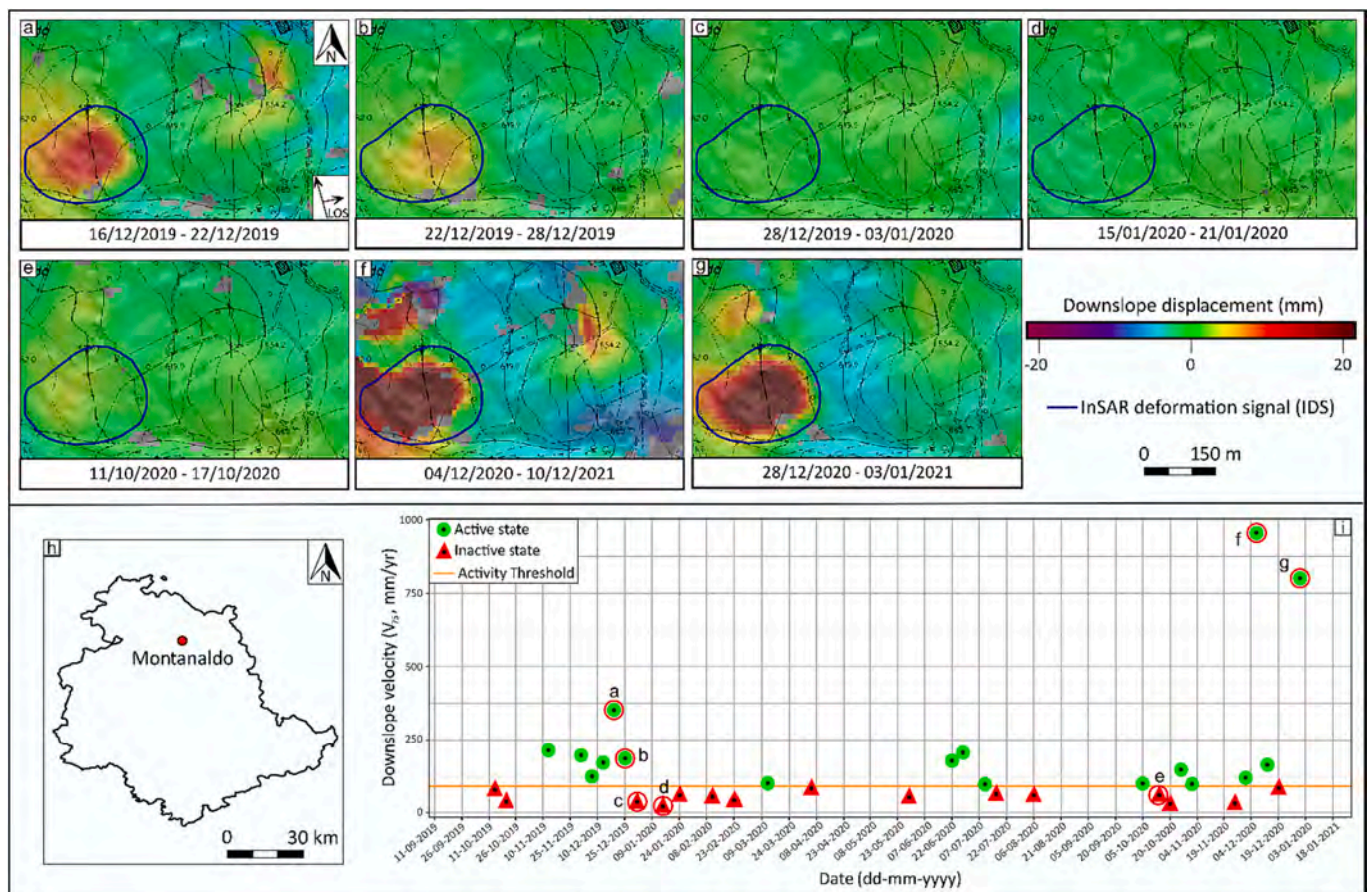

Fig. 10. Example of 6-day interferograms for the Montanaldo IDS illustrating different states of activity (a-g). Velocity time series (i) reports V_{75} obtained from interferograms. Symbols with labels refer to the example interferograms. Location of the landslide on the regional territory shown at the bottom left (h).

during the spring-summer period, possibly due to the favourable W orientation of the slope and/or type of crop and agricultural practices. As in Coldivecchio (Fig. 6), single interferograms occasionally show negative downslope displacement values (Fig. 10f, g) interpreted as artefacts due to residual errors which cannot be eliminated through filtering.

The area characterized by more intense deformations, in this case, is the one located at lower elevations, but evidence of deformations is not lacking even in the upper part of the slope. Fig. 11 shows the extent of the mapped landslide and of the IDS; the UAV photo captures irregular morphology with frequent local counter slopes. In addition, in this case, agricultural practices erase other morphological evidence of movement
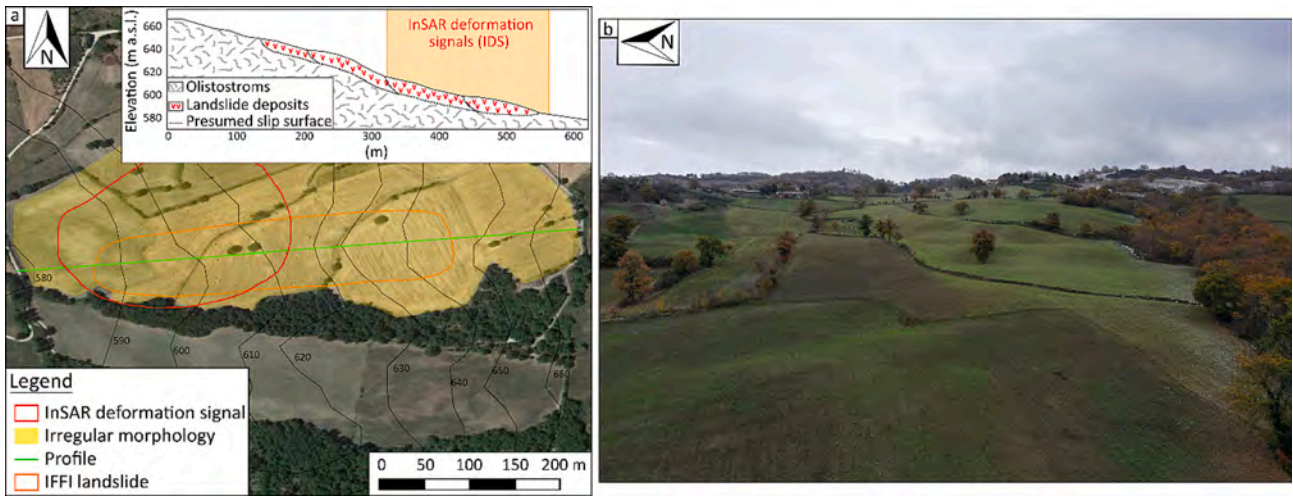
Fig. 11. Schematic map of the slope (left) with aerial photograph showing the perimeters of the mapped landslide and of the IDS. UAV (Unmanned Aerial Vehicle) photograph for the case study "Montanaldo" (right): although the slope is characterized by cultivated fields, the irregular morphology of the slope and the presence of reverse slopes is recognizable.
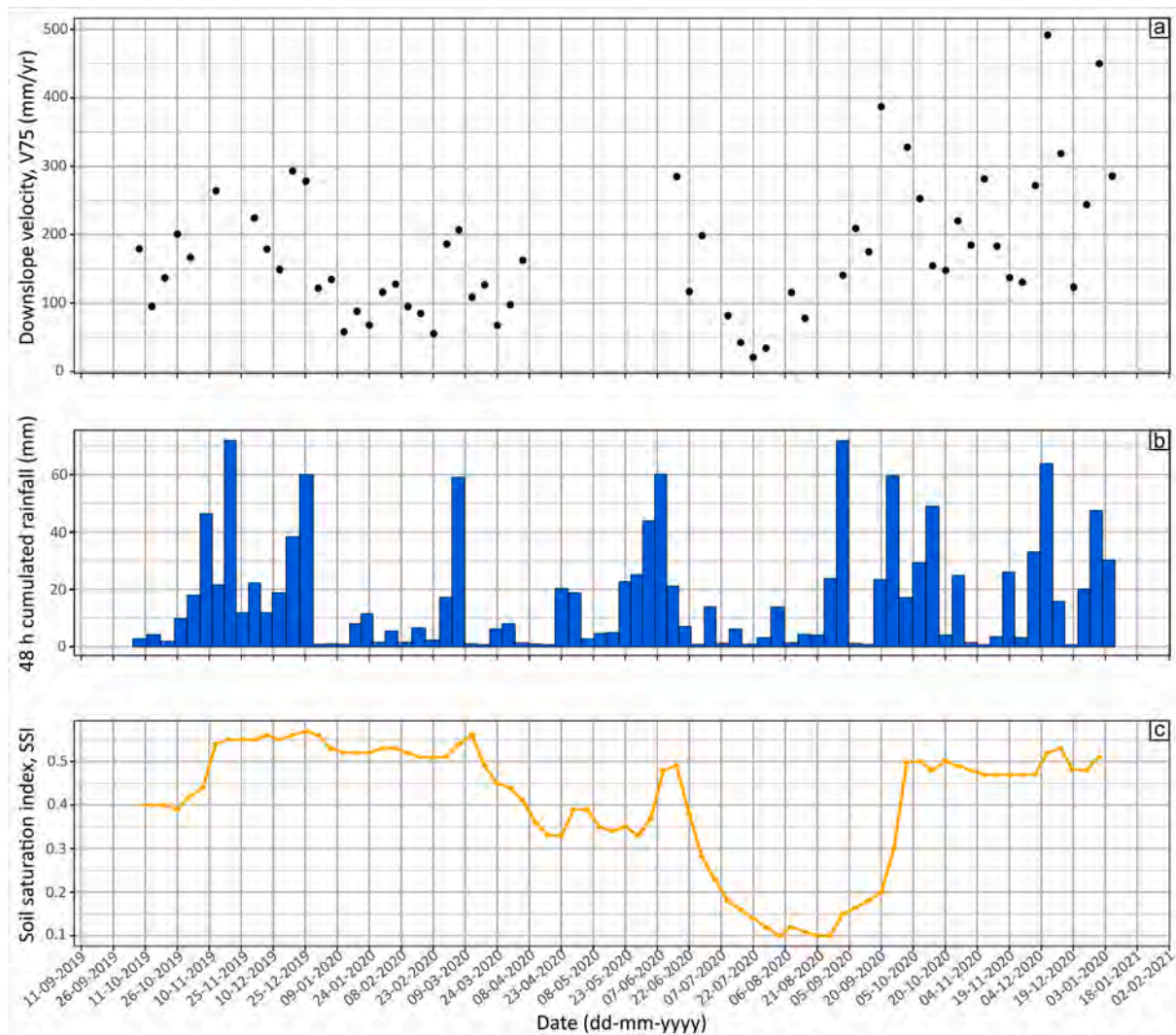

Fig. 12. Comparison between averaged values of IDS velocities, V_{75} (a), 48-h rainfall (b) and SSI (c).

such as small scarps and fractures.

For all three case studies shown within this section, and all the remaining 10 selected IDSs, the field evidence of deformation is rarely evident given the most common land use is agricultural. However, upon site inspection, we invariably found features, such as irregular morphology with occasional counter slopes, water ponding and cracks along roads, which are compatible with ongoing deformations. The InSAR standard analysis produces good quality interferograms, especially during the cold season. The rapid growth of vegetation and the cultivation for agricultural purposes of the areas during the spring-summer season, typically deteriorate the quality of interferograms introducing significant decorrelation.

4.4. Comparison of landslide velocity, 48-h rainfall and soil moisture index

By visually inspecting interferograms, we gain the perception that major rainfall events cause the velocities of IDSs to increase. More particularly, multiple IDSs show relatively high velocities following significant rainfall events that hit the area during the study period (October 2019 to January 2021). In order to verify our qualitative observations, we average velocity time series (V_{75}TS) of 13 selected IDSs and compare them to corresponding averaged values of rainfalls and SSI in Fig. 12. The following observations can be done:

- During October 2019, averaged V_{75} are lower than 200 mm/yr in association to moderate SSI values and no relevant rainfalls.
- During November 2019, rainfalls cause the increase of SSI and available velocities show some increase despite decorrelation problems limiting their retrieval.
- In mid-December, heavy rainfalls and high SSI values are associated with averaged V_{75} of about 300 mm/yr and clearly visible displacements signals in many cases.
- During January and February 2020, very scarce precipitation is associated to a decrease of averaged velocities.
- At the beginning of March, the SSI is still relatively high and rainfalls cause a clear acceleration of IDSs, which translates into averaged V_{75} increasing from 50 to 200 mm/yr approx.
- The spring and summer season record low precipitation values, decreasing SSI and highly decorrelated interferograms which translate into missing values of averaged velocities in Fig. 12a. The effects of the rains occurred during the first half of June, therefore, cannot be evaluated.
- Finally, the two saturation and rainfall peaks of early and late December 2020 are well correlated with IDS acceleration in interferograms and averaged V_{75} reaching peaks of about 500 mm/yr.

In Fig. 13, we report climate-dependent parameters together with

InSAR-derived velocities for the IDS of Case Basse, Coldivecchio and Montanaldo that were previously described (see Section 4.3). Green circles correspond to active state of IDS deformation while magenta circles represent inactive state (see Section 3.3). The diameter of green circles is proportional to the downslope velocity (V_{75}) of the IDS.

Active and inactive IDS states show a good degree of separation in the SSI – 48-h rain space though there are some exceptions. In particular, some active signals plot in the lower part of the graph where *max48rain* is very low. This may happen when, following a reactivation, displacement rates slowly decrease over time before the mass stops (Cascini et al., 2014; Lacroix et al., 2020; Leroueil et al., 1996). The opposite is rarely seen and the upper right part of the chart is mainly populated by active states.

Given that SSI and max48rain are available for the same area and period of the InSAR analysis, we can compare the alert thresholds of the LEWS to all rainfall and soil conditions associated to remotely estimated state of activity of the selected slopes. Conceptually, such comparison allows evaluating the separation of climatic conditions that have and have not resulted in landslide activity (Berti et al., 2012), and check the position of alert thresholds in use for the regional LEWS in such context. Our comparison considers only 13 unstable slopes and a limited time-span; therefore, results intend to provide partial indications together with exploring the suitability of traditional two-pass interferometry for this purpose.

The chart reported in Fig. 14 reports available data for the 13 selected IDSs and the alert thresholds for comparison. The first level alert threshold is described by the following polynomial equation:

$$max24rain = 69.16 \cdot SSI^2 - 130.3 \cdot SSI + 82.64 \qquad (1)$$

In general, the results confirm the good relationship between the InSAR-based landslide activity classification and the climatic parameters (*SSI-max48rain*) used in the Umbria LEWS (Fig. 14a). The area of the chart pertaining to low values of soil saturation (SSI < 0.35 approx.) represents the late spring and summer seasons. Despite being scarcely populated due to frequent highly decorrelated interferograms, the majority of available info indicate inactive states. The opposite is observed in the wet area of the chart where rainfalls operate some discrimination in relation to the velocity of IDSs.

The tools of binary classification metrics can be used to analyse the results of the comparison. Climatic parameters associated to active IDSs describe a true positive (tp) or a false negative (fn) case when above or below the *SSI-max48rain* threshold. In the case of inactive IDSs, they correspond to false positive (fp) cases when above the threshold and true negative (tn) cases, conversely. In the upper, above-threshold portion of the chart, the separation between inactive and active states is clear: only 13 interferograms document inactive states (fp) compared to 99 indicating activity (tp). Below the alert threshold, the data describing active state of movement (i.e., the interferogram shows high displacement
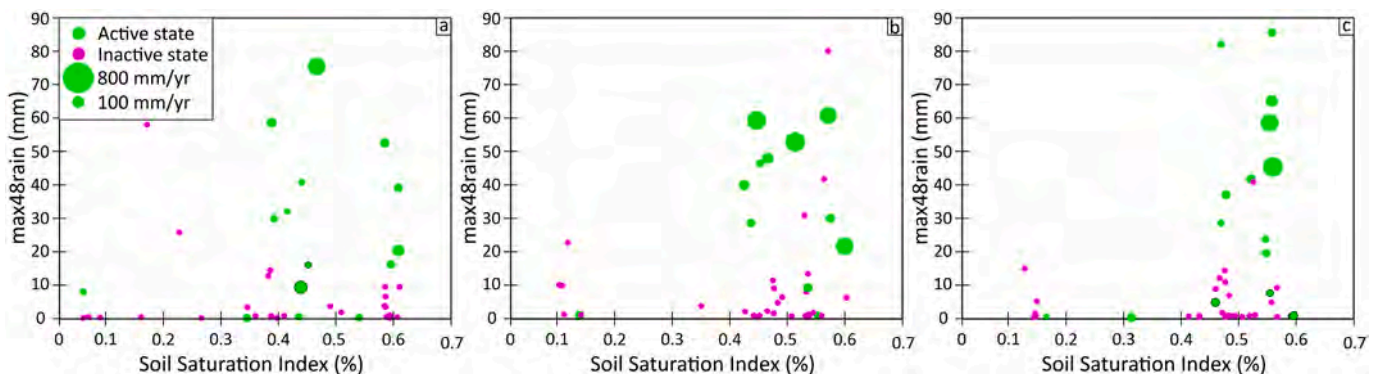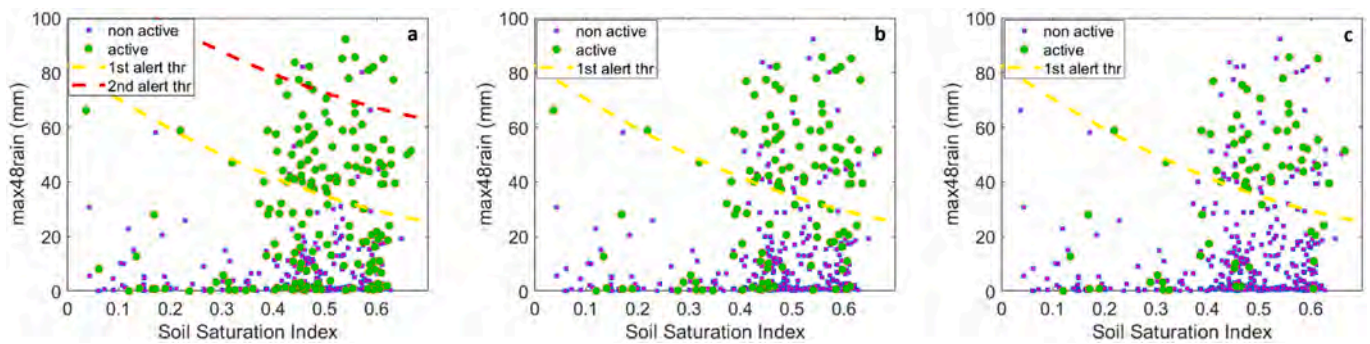

Fig. 13. Distribution of landslide activity states inferred from interferogram analysis in the SSI-max48rain space for the IDS of Case Basse, Coldivecchio e Montanaldo.

Fig. 14. Comparison between IDS state of activity and 1st level alert threshold (yellow) of the Umbria region. (a) state of activity derived from interpreted V_{75} limit value. (b) $1.5\times$ limit value (c) and $2\times$ limit value. (For interpretation of the references to colour in this figure legend, the reader is referred to the web version of this article.)

rates despite the climatic condition didn't exceed the alert threshold). Here, we find 89 interferograms that document active state (fn) compared to 250 inactive (tn). As aggregate measures of performance, here we use the accuracy (acc) which considers both positive and negative true predictions in relation to the total number of cases; the Jouden's J score or bookmaker informedness (bm) which uses true positive and true negative rates and the treat score (CSI) which favours true predictions (Table 3).

The 1st level landslide alert threshold is intended to predict the possibility of landslide occurrence/reactivation over a given territory. The occurrence of a landslide causes significant surface deformation, likely associated to visible damages. Our analysis implicitly assumes that landslide accelerations are triggered by climatic factors (Lacroix et al., 2020; Matsuura et al., 2008) and that increasing displacement rates may precede failure episodes (Carlà et al., 2017; Squarzoni et al., 2020; Scoppettuolo et al., 2020; Zhu et al., 2021). This way, interferometric results describing relatively low displacement rates (30 to 1000 mm/yr approx.) can be used as a proxy of increasing failure probability. In this framework, the choice of the V_{75} limit value for landslide activity classification (see Section 3.3) is crucial. In order to explore its role, we analyse the scenarios generated by using an increasing multiplier for the V_{75} limits. Results are reported in Fig. 14, in the SSI-*max48rain* space, and in Table 4 in terms of the corresponding binary metrics. The number of active cases reduces in favour of inactive ones, which translate in a decrease of tp and fn in favour of fp and tn. In terms of threshold performance, the sensitivity of the model [tp/(tp + fn)] increases while its precision [tp/(tp + fp)] decreases with aggregate measures describing such complex outcome. When both positive and negative predictions are considered, the performance increase (acc) or maintain stable (bm) while it decreases if only positive predictions are considered (CSI), due

Table 4
Contingencies (tp, fp, tn, fn) and skill scores (CSI, bm, acc) for increasing V75 limit values used to classify active and inactive IDSs.

V_{75} limit value multiplier	tp	fp	tn	fn	Threat score CSI	Jouden's J bm	Accuracy acc
1	98	14	249	90	0.485	0.468	0.769
1.5	72	40	286	53	0.4364	0.4533	0.7938
2	47	65	315	24	0.3456	0.491	0.803

to drop in precision that is not balanced by the improved negative prediction (higher tn and lower fn).

The receiving operating characteristics (ROC) method (Swets, 1988) can be used to describe the performance of the SSI-max48rain threshold. For this purpose, we computed ROC curves and optimal skill scores by varying the c parameter (intercept) of Eq. (1) while keeping the other two parameters constant (a = 69.16, b = −130.3). ROC curves, optimal skill scores (Table 3) and associated intercept values were calculated for increasing multiplier of the V_{75} classification limits (0.75 to 2). Results are reported in Fig. 15 where it can be seen that higher multipliers improve accuracy (acc) and diminish the critical success index (CSI) indicating that the prediction of true positive cases tends to worsen while true negative predictions improve. DIS and bm show little variations for the above reason. The single ROC curves are very similar each other as testified by AUC values (Area under the curve, aggregate measure of performance across all possible thresholds described by Eq. (1)) varying between 0.74 and 0.79. Based on our results, the selection of the optimal threshold (Guzzetti et al., 2020) separating climatic conditions that have and have not resulted in landslide activity is not straightforward. Different performance metrics can give different indication and any choice has to take into account the objectives of the threshold. In the following section, we are discussing this topic in more detail.

The evolution of IDS deformation can be visualized by representing the state of activity and V_{75} values for all selected IDSs through time (Fig. 16). Here, we positioned the main 1st level (yellow) and 2nd level (orange) alerts occurred during the period of investigation. Both levels of alert are part of the same regional LEWS and describe a predictive scenario associated to an increasing number of landslides affecting the territory. Fig. 16 allows appreciating when non-active landslides reactivate and when active landslides increase their displacement rate (or the opposite). From our point of view, the evolutionary trend of the unstable slopes is more important than the absolute value of the displacement rate. This latter varies depending on a variety of factors (e. g., type of movement and involved material, style of activity). Furthermore, it is estimated by differential interferometry that is one-dimensional by its own nature and gives results that are influenced by the relative orientation of the movement and the LOS.
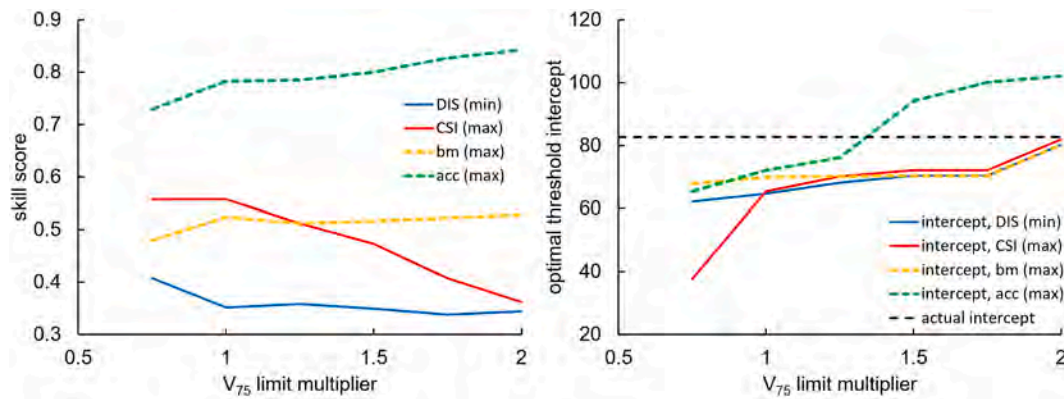
Table 3
Skill scores based on contingencies used to describe the performance of the 1st level alert threshold (tp, true positives; tn, true negative; fp, false positives; fn, false negatives).

Skill score	Formula	Range	Optimal value
Critical success index (threat score)	$CSI = \dfrac{tp}{tp + fn + fp}$	0–1	1
Jouden's J (bookmaker informedness)	$bm = \dfrac{tp}{tp + fn} + \dfrac{tn}{tn + fp} - 1$	−1-1	1
Accuracy	$acc = \dfrac{tp + tn}{tp + tn + fp + fn}$	0–1	1
Distance from the upper left corner of the ROC space	$DIS = \sqrt{\left(1 - \dfrac{tp}{tp + fn}\right)^2 + \left(\dfrac{fp}{fp + tn}\right)^2}$	0–1	0

Fig. 15. Optimal skill scores as a function of the multiplier of the V75 classification limit (a) and associated intercepts of the 1st level alert threshold (b).
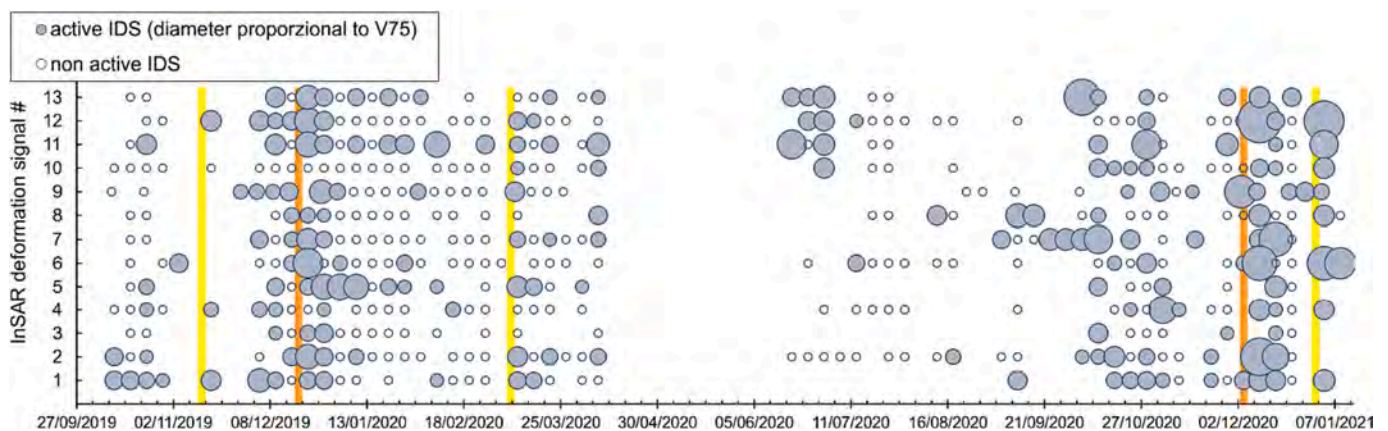

Fig. 16. Overall distribution over time of active (filled circles) and non-active (empty circles) IDS compared to 1st and 2nd level landslide alerts (yellow and orange, respectively) issued by the Umbria region during the study period. (For interpretation of the references to colour in this figure legend, the reader is referred to the web version of this article.)

During the first yellow alert event of November 2019, the scarcity of interferometric information due to widespread decorrelation (see Section 3.1) partially hampers the comparison. However, three out of four available IDS are active. In the following, the number of reactivations/accelerations detected through InSAR during or shortly after the most severe yellow alerts and orange alerts declared by the Functional Centre can be considered as useful experimental evidence validating the 2 alert thresholds used in the Umbria LEWS.

5. Discussion and conclusions

By using the conventional two-pass differential InSAR technique on the territory of the Umbria region, we detected 252 active landslides during the period between October 2019 and January 2021.

Our results show that interferometric stacking represents the most suitable tool for landslide detection and mapping in rural areas. As previously reported by other authors (Handwerger et al., 2015; Dini et al., 2019), it increases the signal-to-noise ratio and highlights features that are persistent in time and space. In the mountain territory of our study area (2480 km^2), dominated by low-gradient slopes, it produces quasi-continuous displacement maps which allow the detection of sustained slow movements over the territory. C-band interferometry, however, may result in poorer coverage of the territory where the terrain is steeper and/or heavily vegetated. We mostly used short temporal baseline IFs (6 to 24 days) to take full advantage of the short revisit time of the Sentinel 1 satellites. The use of short IFs substantially reduce decorrelation and help to get information not only for stable scatterers (i.e., buildings, unvegetated soil and rock outcrops) but also along

moderately vegetated and cultivated slopes, that are most represented in the Umbria region. Short IFs also raise the range of measurable displacement rates in the order of tens to hundreds mm/yr which far exceed the velocities typically measured by multi-temporal InSAR (Solari et al., 2020). We cannot verify the completeness of our IDS inventory, given there is no comparable ground data, and it is possible that some slope movements went undetected. Similarly, we cannot exclude that a careful ground investigation may reveal that some IDS correspond to ground displacements not associated to landsliding. Unfavourable conditions are represented by movements of small extension (< 0.2 km^2 approx.), particularly steep slopes, slopes facing north or south, and areas covered by dense vegetation.

By analysing our InSAR deformation signals (IDS) we find that they are numerically scarce when compared to mapped landslides (about 2%). Also, a significant number (86/252) is positioned along slopes where no landslide is mapped, indicating the potential of InSAR to identify slope deformations which may correspond to undetected landslides or incipient slope failures, thus complementing geomorphological observation for the compilation of landslide inventories. East and West slope exposures favour the detection of IDSs, due to the geometry of satellite observation. The majority of our IDSs are positioned along slopes made of fine-grained weak lithologies where slope gradients range between 7 and 17°, reflecting the landslide susceptibility of the territory. Field surveys confirmed that all the IDS identified are associated to ongoing slope movements. Agricultural practices often hide the evidence of deformation, but irregular morphologies including counter slopes, cracks and damages to the surrounding roads and local water ponding all confirm the remotely sensed information.

The analysis of stacked interferograms to detect and map active slope movements proved well suited for territorial management purposes. It shows good price – quality ratio, performs well in defining the geometry of landslides even in absence of PS, looks like an efficient way to update existing landslide inventories, and to obtain a valuable database, given the costs of field-based monitoring networks. However, unlike multi-temporal InSAR, the accuracy of displacement rates revealed by stacked interferograms is not comparable to ground-based monitoring and the results should be given a qualitative meaning. Only the comparison with proper measurements can determine the level of accuracy which may vary depending on a number of factors (ground reflectivity, DEM precision, slope geometry, …).

The visual inspection of single differential interferograms allow appreciating variable IDS displacement rates that can be used to monitor the state of activity of unstable slopes. We analyzed 6-days IFs, pertaining to 13 selected cases, to extract information about the temporal evolution of ongoing slope deformation. Not all IFs can be used due to decorrelation, and interpretation is required for appropriate selection. This need has obvious consequences on the possibility to apply automatic procedures, but research efforts are starting to address similar problems (Fu et al., 2022). However, results are encouraging, and selected IFs capture the main seasonal variation and the response to major rainfall episodes. The numerical description is entrusted to the 75th percentile of the downplope-projected InSAR-derived velocity within the IDS (V_{75}). Given we use C-band (5.6 cm wavelength) SAR images and 6-days IFs, we theoretically expect to measure displacements rates in the range 15 to 1500 mm/yr. Our V_{75} vary between 30 mm/yr and 1000 mm/yr approximately. Signals below the lower limit cannot be clearly distinguished from stable slopes on 6-days IFs, therefore they are of no practical use.

We compared our results to the landslide early warning system (LEWS) operational in the Umbria region. The system relies upon 1st and 2nd level alert thresholds based on climatic parameters and describing the increasing possibility of having landslide phenomena in a given area of alert. In the case of geographical LEWS, the lack of accurate and reasonably complete information on where and when landslides occur limits greatly the ability to verify the forecasts quantitatively (Guzzetti et al., 2020). Remotely sensed data can help to address such issue (Mondini et al., 2021) and our comparison of two-pass differential interferometry results and alert thresholds aims to explore such possibility.

Our data indicate that the 1st level operational threshold of the Umbria geographical LEWS is capable of identifying the climatic conditions associated to landslide activity detected through InSAR. We do not expect that the comparison exhibits a perfect match because: i) the threshold aims at areal landslide prediction and ii) binary classification of active and non-active landslides through InSAR implies certain simplifications (see Section 4). However, conventional binary classification metrics yield accuracy values (*acc*) of 0.77÷0.81 and Youden's indexes (*bm*) of 0.48-0.51 (Table 4) that indicate the goodness of the threshold predictive performance.

The results indicate that conventional two-pass differential interferometry can provide useful information for geographical LEWS validation. They can effectively contribute to quantify the uncertainties associated to threshold models used for geographical LEWS that, otherwise, are rarely defined (Brunetti et al., 2010).

In the case of the Umbria region, the encouraging results obtained with a limited InSAR dataset indicate that, by increasing the number of InSAR deformation signals and the extension of the analysis period, the analysis is capable to detect and monitor the evolution of active gravitational slope movements over the regional territory.

Finally, thanks to the short revisit time of Sentinel 1 satellites, that we hope will soon be restored to its full 6-days potential, it is possible to imagine a joint use of differential interferogram analysis and geographical LEWS where cross-comparison may improve predictive capabilities.

CRediT authorship contribution statement

Francesco Ponziani: Conceptualization, Investigation, Methodology. **Pierpaolo Ciuffi:** Data curation, Investigation, Visualization, Writing – original draft. **Benedikt Bayer:** Data curation, Methodology. **Nicola Berni:** Conceptualization, Methodology. **Silvia Franceschini:** Data curation, Methodology. **Alessandro Simoni:** Conceptualization, Investigation, Writing – original draft, Writing – review & editing.

Declaration of Competing Interest

The authors declare that they have no known competing financial interests or personal relationships that could have appeared to influence the work reported in this paper.

Data availability

Data will be made available on request.

Appendix A. Supplementary data

Supplementary data to this article can be found online at https://doi.org/10.1016/j.enggeo.2023.107352.

References

Albano, M., Saroli, M., Montuori, A., Bignami, C., Tolomei, C., Polcari, M., Pezzo, G., Moro, M., Atzori, S., Stramondo, S., Salvi, S., 2018. The relationship between InSAR coseismic deformation and earthquake-induced landslides associated with the 2017 Mw 3.9 Ischia (Italy) Earthquake. Geosciences 2018 (8), 303. https://doi.org/10.3390/geosciences8080303.

Bekaert, D.P.S., Handwerger, A.L., Agram, P., Kirschbaum, D.B., 2020. InSAR-based detection method for mapping and monitoring slow-moving landslides in remote regions with steep and mountainous terrain: an application to Nepal. Remote Sens. Environ. 249 (2020), 111983. ISSN 0034–4257. https://doi.org/10.1016/j.rse.2020.111983.

Berti, M., Martina, M.L.V., Franceschini, S., Pignone, S., Simoni, A., Pizziolo, M., 2012. Probabilistic rainfall thresholds for landslide occurrence using a Bayesian approach. J. Geophys. Res. 117, F04006. https://doi.org/10.1029/2012JF002367.

Bezak, N., Jemec Auflič, M., Mikoš, M., 2021. Reanalysis of soil moisture used for rainfall thresholds for rainfall-induced landslides: the Italian case study. Water 13, 1977. https://doi.org/10.3390/w13141977.

Bonham-Carter, G.F., 1994. Geographic Information Systems for Geoscientists: Modeling with GIS. Pergamon Press, Canada.

Brocca, L., Barbetta, S., Melone, F., Moramarco, T., 2010a. A continuous rainfall–runoff model derived from investigations on a small experimental basin. IAHS Publ. 336, 179–185.

Brocca, L., Melone, F., Moramarco, T., Wagner, W., Hasenauer, S., 2010b. ASCAT Soil Wetness Index validation through in-situ and modeled soil moisture data in Central Italy. Remote Sens. Environ. 114 (11), 2745–2755.

Brunetti, M.T., Peruccacci, S., Rossi, M., Luciani, S., Valigi, D., Guzzetti, F., 2010. Rainfall thresholds for the possible occurrence of landslides in Italy. Nat. Hazards Earth Syst. Sci. 10, 447–458. www.nat-hazards-earth-syst-sci.net/10/447/2010/.

Bruno, G., Pignone, F., Silvestro, F., Gabellani, S., Schiavi, F., Rebora, N., Giordano, P., Falzacappa, M., 2021. Performing hydrological monitoring at a national scale by exploiting rain-gauge and radar networks: the Italian case. Atmosphere 12, 771. https://doi.org/10.3390/atmos12060771.

Bürgmann, R., Rosen, P.A., Fielding, E.J., 2000. Synthetic aperture radar interferometry to measure Earth's surface topography and its deformation. Annu. Rev. Earth Planet. Sci. 28, 169–209.

Cardinali, M., Reichenbach, P., Guzzetti, F., Ardizzone, F., Antonini, G., Galli, M., Cacciano, M., Castellani, M., Salvati, P., 2002. A geomorphological approach to the estimation of landslide hazards and risks in Umbria, Central Italy. Nat. Hazards Earth Syst. Sci. 2, 57–72. https://doi.org/10.5194/nhess-2-57-2002.

Carlà, T., Intrieri, E., Di Traglia, F., Nolesini, T., Gigli, G., Casagli, N., 2017. Guidelines on the use of inverse velocity method as a tool for setting alarm thresholds and forecasting landslides and structure collapses. Landslides 14 (2), 517–534. https://doi.org/10.1007/s10346-016-0731-5.

Cascini, L., Calvello, M., Grimaldi, G.M., 2014. Displacement trends of slow-moving landslides: classification and forecasting. J. Mt. Sci. 11 (3), 592–606. https://doi.org/10.1007/s11629-013-2961-5.

Chae, B.-J., Park, H.-J., Catani, F., Simoni, A., Berti, M., 2017. Landslide prediction, monitoring and early warning: a concise review of state-of-the-art. Geosci. J. 21 (6), 1033–1070. https://doi.org/10.1007/s12303-017-0034-4.

Chen, C.W., Zebker, H.A., 2001. Two-dimensional phase unwrapping with use of statistical models for cost functions in nonlinear optimization. JOSA A 18, 338–351.

Ciuffi, P., Bayer, B., Berti, M., Franceschini, S., Simoni, A., 2021. Deformation detection in cyclic landslides prior to their reactivation using two-pass satellite interferometry. Appl. Sci. 11, 3156. https://doi.org/10.3390/app11073156.

Cohen-Waeber, J., Bürgmann, R., Chaussard, E., Giannico, C., Ferretti, A., 2018. Spatiotemporal patterns of precipitation-modulated landslide deformation from independent component analysis of InSAR time series. Geophys. Res. Lett. 45 (4), 1878–1887. https://doi.org/10.1002/2017GL075950.

Dini, B., Manconi, A., Loew, S., 2019. Investigation of slope instabilities in NW Bhutan as derived from systematic DInSAR analyses. Eng. Geol. 259, 105111.

Dong, J., Zhang, L., Li, M., Yu, Y., Liao, M., Gong, J., Luo, H., 2018. Measuring precursory movements of the recent Xinmo landslide in Mao County, China with Sentinel-1 and ALOS-2 PALSAR-2 datasets. Landslides 15, 135–144. https://doi.org/10.1007/s10346-017-0914-8.

Froude, M.J., Petley, D., 2018. Global fatal landslide occurrence from 2004 to 2016. Nat. Hazards Earth Syst. Sci. 18 (8), 2161–2181. https://doi.org/10.5194/nhess-18-2161-2018.

Fu, L., Zhang, Q., Wang, T., Li, W., Xu, Q., Ge, D., 2022. Detecting slow-moving landslides using InSAR phase-gradient stacking and deep-learning network. Front. Environ. Sci. 10, 963322 https://doi.org/10.3389/fenvs.2022.963322.

Gariano, S.L., Guzzetti, F., 2016. Landslides in a changing climate. Earth Sci. Rev. 162, 227–252. https://doi.org/10.1016/j.earscirev.2016.08.011.

Glade, T., Crozier, M.J., 2005. The nature of landslide Hazard impact. In: Landslide Hazard and Risk, 41–74. John Wiley & Sons Ltd, Chichester, England, p. 2005.

Goldstein, R.M., Werner, C.L., 1998. Radar interferogram filtering for geophysical applications. Geophys. Res. Lett. 25, 4035–4038.

Guzzetti, F., 2000. Landslide fatalities and the evaluation of landslide risk in Italy. Eng. Geol. 58 (2), 89–107. https://doi.org/10.1016/S0013-7952(00)00047-8.

Guzzetti, F., Mondini, A.C., Cardinali, M., Fiorucci, F., Santangelo, M., Chang, K.T., 2012. Landslide inventory maps: New tools for an old problem. Earth Sci. Rev. 112 (1–2), 42–66.

Guzzetti, F., Gariano, S.L., Peruccacci, S., Brunetti, M.T., Marchesini, I., Rossi, M., Melillo, M., 2020. Geographical landslide early warning systems. Earth Sci. Rev. 102973.

Handwerger, A.L., Roering, J.J., Schmidt, D.A., 2013. Controls on the seasonal deformation of slow-moving landslides. Earth Planet. Sci. Lett. 377, 239–247.

Handwerger, A.L., Roering, J.J., Schmidt, D.A., Rempel, A.W., 2015. Kinematics of earthflows in the northern California coast ranges using satellite interferometry. Geomorphology 246, 321–333.

Hilley, G.E., Bürgmann, R., Ferretti, A., Novali, F., Rocca, F., 2004. Dynamics of slow-moving landslides from permanent scatterer analysis. Science 304 (5679), 1952–1955.

Hu, X., Bürgmann, R., Lu, Z., Handwerger, A.L., Wang, T., Miao, R., 2019. Mobility, thickness, and hydraulic diffusivity of the slow-moving monroe landslide in California Revealed by L-Band satellite radar interferometry. J. Geophys. Res. Solid Earth 124, 7504–7518.

Hungr, O., Leroueil, S., Picarelli, L., 2014. The Varnes classification of landslide types, an update. Landslides 11, 167–194. https://doi.org/10.1007/s10346-013-0436-y.

Kishore, N., Marqués, D., Mahmud, A., Kiang, M., Rodriguez, I., et al., 2018. Mortality in Puerto Rico after Hurricane Maria. N. Engl. J. Med. 379 (2), 162–170. https://doi.org/10.1056/NEJMsa1803972.

Lacroix, P., Handwerger, A.L., Bièvre, G., 2020. Life and death of slow-moving landslides. Nat. Rev. Earth Environ. 1, 404–419. https://doi.org/10.1038/s43017-020-0072-8.

Lazzari, M., Piccarreta, M., Manfreda, S., 2018. The role of antecedent soil moisture conditions on rainfall-triggered shallow landslides. Nat. Hazards Earth Syst. Sci. Discuss. https://doi.org/10.5194/nhess-2018-371 [preprint].

Leroueil, S., Locat, J., Vaunat, J., Picarelli, L., Lee, H., Faure, R., 1996. Geotechnical characterization of slope movements. In: Senneset, K. (Ed.), Landslides, Proceedings 7th International Symposium Landslides, Trondheim, Norway, 17–21 June, 1, pp. 53–74. Balkema, Rotterdam, The Netherlands.

Liang, C., Liu, Z., Fielding, E.J., Bürgmann, R., 2018. InSAR time series analysis of L-Band wide-swath SAR data acquired by ALOS-2. IEEE Trans. Geosc. Remote Sens. 56 (8), 4492–4506. AUGUST 2018.

Manconi, A., 2021. How phase aliasing limits systematic space-borne DInSAR monitoring and failure forecast of alpine landslides. Eng. Geol. 287, 106094 https://doi.org/10.1016/j.enggeo.2021.106094.

Mantovani, F., Soeters, R., Van Westen, C.J., 1996. Remote sensing techniques for landslide studies and hazard zonation in Europe. Geomorphology 15, 213–225. https://doi.org/10.1016/0169-555X(95)00071-C.

Massonnet, D., Feigl, K.L., 1998. Radar interferometry and its application to changes in the Earth's surface. Rev. Geophys. 36, 441–500.

Matsuura, S., Asano, S., Okamoto, T., 2008. Relationship between rain and/or meltwater, pore-water pressure and displacement of a reactivated landslide. Eng. Geol. 101, 49–59.

Meyer, N.K., Schwanghart, W., Korup, O., Romstad, B., Etzelmüller, B., 2014. Estimating the topographic predictability of debris flows. Geomorphology 207, 114–125. https://doi.org/10.1016/j.geomorph.2013.10.030.

Mondini, A.C., Guzzetti, F., Chang, K.-T., Monserrat, O., Martha, T.R., Manconi, A., 2021. Landslide failures detection and mapping using synthetic aperture radar: past, present and future. Earth Sci. Rev. 216, 103574 https://doi.org/10.1016/j.earscirev.2021.103574.

Murray, K.D., Bekaert, D.P.S., Lohman, R.B., 2019. Tropospheric corrections for InSAR: Statistical assessments and applications to the Central United States and Mexico. Remote Sens. Environ. 232, 111326.

Peruccacci, S., Brunetti, M.T., Gariano, S.L., Melillo, M., Rossi, M., Guzzetti, F., 2017. Rainfall thresholds for possible landslide occurrence in Italy. Geomorphology 290, 39–57. https://doi.org/10.1016/j.geomorph.2017.03.031.

Pialli, G., Plesi, G., Damiani, A.V., Brozzetti, F., 2009. Note illustrative della Carta Geologica d'Italia alla scala 1:50.000, Foglio N. 289 Città di Castello, Selca, Firenze.

Ponziani, F., Pandolfo, C., Stelluti, M., Berni, N., Brocca, L., Moramarco, T., 2012. Assessment of rainfall thresholds and soil moisture modeling for operational hydrogeological risk prevention in the Umbria region (Central Italy). Landslides 9, 229–237.

Raspini, F., Bianchini, S., Ciampalini, A., Del Soldato, M., Montalti, R., Solari, L., Tofani, V., Casagli, N., 2019. Persistent Scatterers continuous streaming for landslide monitoring and mapping: the case of the Tuscany region (Italy). Landslides 16, 2033–2044.

Regmi, N.R., Giardino, J.R., Vitek, J.D., 2010. Modeling susceptibility to landslides using the weight of evidence approach: Western Colorado, USA. Geomorphology 115 (1–2), 172–187. https://doi.org/10.1016/j.geomorph.2009.10.002.

Sandwell, D., Mellors, R., Tong, X., Wei, M., Wessel, P., 2011. Open radar interferometry software for mapping surface deformation. EOS Trans. Am. Geophys. Union 92, 234.

Scoppettuolo, M.R., Cascini, L., Babilio, E., 2020. Typical displacement behaviours of slope movements. Landslides 17, 1105–1116. https://doi.org/10.1007/s10346-019-01327-z.

Shi, X., Zhang, L., Zhong, Y., Zhang, L., Liao, M., 2020. Detection and characterization of active slope deformations with Sentinel-1 InSAR analyses in the Southwest Area of Shanxi, China. Remote Sens. 12, 392. https://doi.org/10.3390/rs12030392.

Silvestro, F., Gabellani, S., Delogu, F., Rudari, R., Boni, G., 2013. Exploiting remote sensing land surface temperature in distributed hydrological modelling: the example of the Continuum model. Hydrol. Earth Syst. Sci. 17, 39–62. https://doi.org/10.5194/hess-17-39-2013, 2013.

Silvestro, F., Gabellani, S., Rudari, R., Delogu, F., Laiolo, P., Boni, G., 2015. Uncertainty reduction and parameter estimation of a distributed hydrological model with ground and remote-sensing data. Hydrol. Earth Syst. Sci. 19, 1727–1751. https://doi.org/10.5194/hess-19-1727-2015, 2015.

Sinclair, S., Pegram, G., 2005. Combining radar and rain gauge rainfall estimates using conditional merging. Atmosph. Sci. Lett. 6, 19–22. https://doi.org/10.1002/asl.85.

Solari, L., Bianchini, S., Franceschini, R., Barra, A., Monserrat, O., Thuegaz, P., Bertolo, D., Crosetto, M., Catani, F., 2020. Satellite interferometric data for landslide intensity evaluation in mountainous regions. Int. J. Appl. Earth Obs. Geoinf. 87, 102028.

Spiegelhalter, D.J., 1986. A statistical view of uncertainty in expert systems. In: Gale, W. (Ed.), Artificial Intelligence and Statistics. Addison-Wesley, Reading, MA, pp. 17–55.

Squarzoni, G., Benedikt, B., Franceschini, S., Simoni, 2020. A Pre- and post-failure dynamics of landslides in the Northern Apennines revealed by space-borne synthetic aperture radar interferometry (InSAR). Geomorphology 369, 107353.

Swets, J.A., 1988. Measuring the Accuracy of Diagnostic Systems. Science 240, 1285–1293. https://doi.org/10.1126/science.3287615.

Tong, X., Schmidt, D., 2016. Active movement of the Cascade landslide complex in Washington from a coherence-based InSAR time series method. Remote Sens. Environ. 186, 405–415.

Trigila, A., Iadanza, C., Spizzichino, D., 2010. Quality assessment of the Italian Landslide Inventory using GIS processing. Landslides 7, 455–470. https://doi.org/10.1007/s10346-010-0213-0.

Wasowski, J., Bovenga, F., 2014. Investigating landslides and unstable slopes with satellite Multi Temporal Interferometry: current issues and future perspectives. Eng. Geol. 174, 103–138. https://doi.org/10.1016/j.enggeo.2014.03.003.

Wicki, A., Lehmann, P., Hauck, C., Seneviratne, S.I., Waldner, P., Stähli, M., 2020. Assessing the potential of soil moisture measurements for regional landslide early warning. Landslides 17, 1881–1896. https://doi.org/10.1007/s10346-020-01400-y.

Xie, M., Zhao, W., Ju, N., He, C., Huang, H., Cui, Q., 2020. Landslide evolution assessment based on InSAR and real-time monitoring of a large reactivated landslide, Wenchuan, China. Eng. Geol. 277, 105781 https://doi.org/10.1016/j.enggeo.2020.105781.

Xu, Y., Lu, Z., Schulz, W.H., Kim, J., 2020. Twelve-year dynamics and rainfall thresholds for alternating creep and rapid movement of the Hooskanaden landslide from integrating InSAR, pixel offset tracking, and borehole and hydrological measurements. J. Geophys. Res. Earth 125, e2020JF005640. https://doi.org/10.1029/2020JF005640.

Yunjun, Z., Fattahi, H., Amelung, F., 2019. Small baseline InSAR time series analysis: Unwrapping error correction and noise reduction. Comput. Geosci. 133, 104331 https://doi.org/10.1016/j.cageo.2019.104331.

Zebker, H.A., Villasenor, J., 1992. Decorrelation in interferometric radar echoes. IEEE Trans. Geosci. Remote Sens. 30, 950–959.

Zhang, Y., Meng, X.M., Dijkstrac, T.A., Jordan, C.G., Chen, G., Zeng, R.Q., Novellino, A., 2020. Forecasting the magnitude of potential landslides based on InSAR techniques. Remote Sens. Environ. 241, 111738.

Zhao, C., Lu, Z., Zhang, Q., de La Fuente, J., 2012. Large-area landslide detection and monitoring with ALOS/PALSAR imagery data over northern California and southern Oregon, USA. Remote Sens. Environ. 124, 348–359.

Zhu, Y., Qiu, H., Yang, D., et al., 2021. Pre- and post-failure spatiotemporal evolution of loess landslides: a case study of the Jiangou landslide in Ledu, China. Landslides 18, 3475–3484. https://doi.org/10.1007/s10346-021-01714-5.